



# CME–CME Interactions as Sources of CME Geoeffectiveness: The Formation of the Complex Ejecta and Intense Geomagnetic Storm in 2017 Early September

Camilla Scolini<sup>1,2</sup> , Emmanuel Chané<sup>1</sup> , Manuela Temmer<sup>3</sup> , Emilia K. J. Kilpua<sup>4</sup> , Karin Dissauer<sup>3</sup> , Astrid M. Veronig<sup>3,5</sup> , Erika Palmerio<sup>4</sup> , Jens Pomoell<sup>4</sup> , Mateja Dumbovic<sup>6</sup> , Jingnan Guo<sup>7,8</sup> , Luciano Rodriguez<sup>2</sup> , and Stefaan Poedts<sup>1,9</sup> 

<sup>1</sup> Centre for mathematical Plasma Astrophysics, Dept. of Mathematics, KU Leuven, B-3001 Leuven, Belgium; [camilla.scolini@kuleuven.be](mailto:camilla.scolini@kuleuven.be)

<sup>2</sup> Solar-Terrestrial Centre of Excellence—SIDC, Royal Observatory of Belgium, B-1180 Brussels, Belgium

<sup>3</sup> Institute of Physics, University of Graz, A-8010 Graz, Austria

<sup>4</sup> Department of Physics, University of Helsinki, FI-00014 Helsinki, Finland

<sup>5</sup> Kanzelhöhe Observatory for Solar and Environmental Research, University of Graz, A-9521 Treffen, Austria

<sup>6</sup> Hvar Observatory, Faculty of Geodesy, University of Zagreb, 10000 Zagreb, Croatia

<sup>7</sup> CAS Key Laboratory of Geospace Environment, School of Earth and Space Sciences, University of Science and Technology of China, 230026 Hefei, People's Republic of China

<sup>8</sup> CAS Center for the Excellence in Planetology, 230026 Hefei, People's Republic of China

<sup>9</sup> Institute of Physics, University of Maria Curie-Skłodowska, PL-20-031 Lublin, Poland

Received 2019 November 14; accepted 2019 December 10; published 2020 February 24

## Abstract

Coronal mass ejections (CMEs) are the primary sources of intense disturbances at Earth, where their *geoeffectiveness* is largely determined by their dynamic pressure and internal magnetic field, which can be significantly altered during interactions with other CMEs in interplanetary space. We analyze three successive CMEs that erupted from the Sun during 2017 September 4–6, investigating the role of CME–CME interactions as a source of the associated intense geomagnetic storm ( $Dst_{\min} = -142$  nT on September 7). To quantify the impact of interactions on the (geo)effectiveness of individual CMEs, we perform global heliospheric simulations with the European Heliospheric Forecasting Information Asset (EUHFORIA) model, using observation-based initial parameters with the additional purpose of validating the predictive capabilities of the model for complex CME events. The simulations show that around 0.45 au, the shock driven by the September 6 CME started compressing a preceding magnetic ejecta formed by the merging of two CMEs launched on September 4, significantly amplifying its  $B_z$  until a maximum factor of 2.8 around 0.9 au. The following gradual conversion of magnetic energy into kinetic and thermal components reduced the  $B_z$  amplification until its almost complete disappearance around 1.8 au. We conclude that a key factor at the origin of the intense storm triggered by the 2017 September 4–6 CMEs was their arrival at Earth during the phase of maximum  $B_z$  amplification. Our analysis highlights how the amplification of the magnetic field of individual CMEs in spacetime due to interaction processes can be characterized by a growth, a maximum, and a decay phase, suggesting that the time interval between the CME eruptions and their relative speeds are critical factors in determining the resulting impact of complex CMEs at various heliocentric distances (*helioeffectiveness*).

*Unified Astronomy Thesaurus concepts:* [Solar coronal mass ejections \(310\)](#); [Solar-terrestrial interactions \(1473\)](#); [Magnetohydrodynamics \(1964\)](#); [Solar wind \(1534\)](#)

*Supporting material:* [animation](#)

## 1. Introduction

Coronal mass ejections (CMEs) are huge eruptions of plasma and magnetic fields from the Sun that propagate through the heliosphere and can eventually impact Earth and other planets and spacecraft. Considered to be the major drivers of strong space weather disturbances at Earth (Gosling et al. 1991; Gosling 1993; Huttunen et al. 2005; Koskinen & Huttunen 2006; Richardson & Cane 2012; Kilpua et al. 2017b), CMEs and their related interplanetary structures (i.e., CME-driven shocks, sheaths, and magnetic ejecta, e.g., Kilpua et al. 2017a) have been found to be responsible for up to 90% of all intense ( $Dst < -100$  nT) geomagnetic storms (Zhang et al. 2007). These intense storms are primarily caused by the combination of long-lasting (typically over 3 hr), strongly southward (negative  $B_z$ ) interplanetary magnetic fields and high dynamic pressure within magnetic ejecta (see, e.g., Tsurutani et al. 1988; Farrugia et al. 1993).

While the majority of these storms are driven by single CMEs (about 60%), a significant fraction (about 27%) is found to be caused by the passage of complex signatures generated by the interaction of individual CMEs with other transients, such as other CMEs and stream interaction regions (Zhang et al. 2007; Vennerstrom et al. 2016). While several studies established that CME–CME interactions are likely to increase the impact on Earth (*geoeffectiveness*) of individual CMEs (see Lugaz et al. 2017, and references therein), the actual quantification of this amplification has been rarely investigated (see, e.g., Xiong et al. 2007, 2009; Shen et al. 2018).

Although the probability of CME–CME interactions in the corona and interplanetary space is higher during periods of maximum solar activity, when the CME occurrence can exceed the rate of 10 CMEs/day (Yashiro et al. 2004; Robbrecht et al. 2009), intense geomagnetic storms caused by CME–CME interactions during activity minima might also occur, most likely in association with sympathetic and (quasi-)homologous

CMEs that erupt from the same active region (AR) (Lugaz et al. 2007, 2017). At the time of this study, the most recent intense geomagnetic storm related to interacting CMEs occurred in early 2017 September, due to the intense negative  $B_z$  generated as a consequence of the propagation of a CME-driven interplanetary shock through a preceding magnetic ejecta. This event was also associated with two of the four most intense X-class solar flares observed in Solar Cycle 24, originating from an AR (NOAA AR 12763) that presented outstanding levels of CME and flare productivity (Chertok et al. 2018; Redmon et al. 2018; Bruno et al. 2019). Shen et al. (2018) investigated the impact of these CMEs on Earth using remote-sensing and in situ observations and estimated an amplification of the geoeffectiveness of the individual CMEs by a factor of  $\sim 2$  due to CME–CME interactions close to 1 au. The evolution of this amplification in space and time as the CMEs propagated from Sun to Earth, as well as its physical origin, remain unclear.

So far, very few studies have attempted to quantify the geoeffectiveness amplification (in terms of  $B_z$  and/or other geomagnetic activity indices) by performing global Sun-to-Earth simulations of real CME events. At the same time, the geoeffectiveness amplification at Earth can be expected to be the result of a gradual amplification developing in spacetime as the CMEs involved propagate from Sun to Earth, as a consequence of the various interaction phases. To the best of our knowledge, no previous study investigating the evolution of this amplification in spacetime was ever performed. In order to address this previously uninvestigated aspect of CME–CME interactions, in this work we therefore introduce new terminology to refer to the amplification of the potential impact of a given CME at a generic location in the heliosphere. Taking the Earth as an example, we consider the magnitude of the north–south magnetic field component  $B_z$  within CMEs as a primary proxy for their potential impact at a generic location in the heliosphere, which we refer to as CME “*helioeffectiveness*.” In the following, the amplification of the CME helioeffectiveness at a generic location space will be quantified in terms of the amplification of the southward  $B_z$  within a given CME as a consequence of CME–CME interaction phenomena.

Since the ultimate impact of CMEs on geospace is largely determined by their internal magnetic configuration at 1 au, studies aiming to assess the helioeffectiveness of CMEs in spacetime and their resulting geoeffectiveness at Earth require the use of global, physics-based models of the heliosphere capable of describing the 3D magnetic field structure of CMEs, usually by means of various classes of flux rope models. Recent advances in the field (see, e.g., Green et al. 2018; Feng 2020, for recent reviews of the available models) include the European Heliospheric Forecasting Information Asset (EUHFORIA; Pomoell & Poedts 2018), which has been extended to model CMEs using a linear force-free spheromak model (Verbeke et al. 2019b). A first test of the predictive capability of this model, limited to noninteracting, single CMEs, has been performed by Scolini et al. (2019), who also developed a basic methodological scheme to determine the complete set of CME kinematical, geometrical, and magnetic parameters from remote-sensing observations of CMEs in the solar corona. The modeling capabilities of the spheromak model in EUHFORIA in the case of complex, interacting CME events, however, have so far remained unexplored. Clearly, in order to ultimately quantify the actual geoeffectiveness

amplification resulting from the interaction of the CMEs and the terrestrial magnetosphere, heliospheric CME evolution models need to be further coupled to a model of the geospace. As the coupling between the EUHFORIA heliospheric model and physics-based global models of the magnetospheric-ionospheric environments is beyond the scope of this work, we leave the assessment of the capabilities of such a model chain for a future study.

The double goal of this study is, therefore, (1) to quantify the increase of the helioeffectiveness (in terms of  $B_z$  amplification) and the geoeffectiveness (in terms of  $B_z$  and Dst index amplification) of individual CMEs due to interaction processes via global, physics-based heliospheric simulations of the specific CME event considered and (2) to test the predictive performances of the EUHFORIA spheromak CME model for complex multi-CME events.

The paper is organized as follows: in Section 2 we introduce the instruments and data used in this work, and we present a complete Sun-to-Earth observational overview of the CMEs under study. In Section 3 we describe the observation-based methods used to derive the CME geometric, kinematic, and magnetic parameters from remote-sensing observations of the CMEs close to the Sun. In Section 4 we introduce the simulations performed and present a detailed analysis of the events comparing observational and modeling results. Finally, in Section 5 we discuss the results and consider future improvements and applications.

## 2. Observations

In this section we describe the observational properties of a series of major CMEs that erupted from the Sun during 2017 September 4–6 and that resulted in a complex and geoeffective signature at Earth on 2017 September 6–9. We start by analyzing white-light coronagraph images of the CMEs taken by the Large Angle and Spectrometric Coronagraph (LASCO; Brueckner et al. 1995) C2 and C3 instruments on board the *Solar and Heliospheric Observatory* (SOHO; Domingo et al. 1995) and by the Sun Earth Connection Coronal and Heliospheric Investigation (SECCHI; Howard et al. 2008) COR2 coronagraph on board the *Solar Terrestrial Relations Observatory* (STEREO; Kaiser et al. 2008)–ahead (A) spacecraft. We then discuss the global characteristics of their (common) source region as observed by the Helioseismic and Magnetic Imager (HMI; Scherrer et al. 2012) and Atmospheric Imaging Assembly (AIA; Lemen et al. 2012) instruments on board the *Solar Dynamics Observatory* (SDO; Pesnell et al. 2012). Finally, we present an overview of the in situ measurements taken at the Sun–Earth Lagrange L1 point by the Magnetic Field Investigation (MFI; Lepping et al. 1995) and the Solar Wind Experiment (SWE; Ogilvie et al. 1995) instruments on board the *Wind* (Ogilvie & Desch 1997) spacecraft and by the *Deep Space Climate Observatory* (DSCOVR; Burt & Smith 2012) spacecraft, discussing the association of the complex in situ signatures with the CME events observed at the Sun.

### 2.1. White-light CME Observations

The first CME (hereafter CME1) was first observed in the LASCO/C2 coronagraph on September 4 at 19:00 UT as a partial halo with a dominant propagation component toward the southwest. It was associated with an M1.7 class flare

(start: 18:46 UT—peak: 19:37 UT—end: 19:52 UT) localized in AR 12673. The CME propagated in LASCO/C2 and LASCO/C3 with an average speed (projected in the plane of sky) of about  $600 \text{ km s}^{-1}$ , exhibiting a slightly accelerating behavior (from the LASCO CME catalog, [https://cdaw.gsfc.nasa.gov/CME\\_list/](https://cdaw.gsfc.nasa.gov/CME_list/)). On the day of the first eruption, *STEREO-A* was separated from Earth by an angle of  $128^\circ$ ; therefore Earth-directed CMEs could be well observed by the COR2 instrument on board *STEREO-A*. In this instrument, the CME was visible starting from 19:39 UT, where it appeared to propagate toward the southwest.

When the leading edge of CME1 was at  $\sim 10$  solar radii ( $R_\odot$ ) as seen by LASCO/C3, it was overtaken by a second, faster CME (hereafter CME2) that was first observed in LASCO/C2 at 20:36 UT. This second CME appeared from Earth as a full halo having an intensified frontal part propagating toward the south, with an average projected speed of about  $1420 \text{ km s}^{-1}$ . CME2 was associated with an M5.5 class flare (start: 20:28—peak: 20:33—end: 20:37) also localized in AR 12673. In *STEREO/COR2-A*, the CME was seen to propagate toward the southwest (first appearance: 20:39 UT), catching up with CME1 shortly after 21:00 UT. By 21:42 UT, the leading edges of CME1 and CME2 had completely merged as seen by LASCO/C3 as well, so that the two structures became indistinguishable in both LASCO and COR2 images. The two CMEs erupted from the same AR less than 2 hr apart and exhibited similar coronal signatures, suggesting a sympathetic, (quasi-)homologous nature (Zhang & Wang 2002; Cheng et al. 2006; Wang et al. 2013).

The day after the eruption of CME1 and CME2 (i.e., September 5), little activity was observed in the LASCO and *STEREO-A* coronagraphs. One faint partial halo CME, most probably also erupting from AR 12673, was visible starting from 17:36 UT in LASCO/C2, but it became too faint to be tracked in the LASCO/C3 field of view. It was at all times barely visible even in running-difference images from *STEREO/COR2-A*, where its front appeared to propagate predominantly below the ecliptic plane. The faintness of this CME in LASCO and *STEREO-A* coronagraph images, combined with the limited eruption signatures visible in EUV images of the solar disk, makes the reconstruction of its kinematic, geometric, and magnetic parameters using the techniques presented in Section 3 particularly complicated. Considering also its propagation direction below the ecliptic plane, we have neglected this event in the following analysis (see also Werner et al. 2019, for a similar modeling approach). However, we point out that this CME could have contributed to the complexity of the event observed at Earth by interacting with the preceding and following CMEs.

Finally, on September 6, a full-halo CME, hereafter CME3, was observed entering the LASCO/C2 field of view at 12:24 UT. This CME originated from the same AR as the previous ones, and it was associated with a remarkably intense flare of class X9.3 (start: 11:53 UT—peak: 12:02 UT—end: 12:10 UT). The CME was observed to propagate toward the southwest with a projected speed of about  $1570 \text{ km s}^{-1}$ , and its leading edge was characterized by a highly elliptical shape tilted by about  $45^\circ$  with respect to the solar equator. In *STEREO/COR2-A* the CME appeared as a full halo (first appearance: 12:24 UT) characterized by a southwest propagation direction (see Appendix A for additional details).

## 2.2. Source Region Observations

The source regions of the CMEs discussed above can all be located within AR 12673. This AR presented outstanding levels of CME and flare productivity persisting for more than a full week (Chertok et al. 2018; Redmon et al. 2018; Bruno et al. 2019). The region was first classified as a simple  $\alpha$  region (Hale et al. 1919; Künzel 1965) on August 30, when it was rotating toward the solar disk center from the eastern limb. It was then classified as  $\beta\gamma$  on September 3, that is, the day before the eruption of CME1. The region then developed into a  $\beta\gamma\delta$  configuration starting from September 5. Figure 1 shows *SDO* observations of the AR as observed by the HMI and AIA instruments.

From September 4 onward, photospheric magnetograms of the AR show the presence of a complex system of polarity inversion lines (PILs) that evolved and rotated over the days (Figures 1(a)–(c)). Two main PIL systems, one in the southeast part of the AR, characterized by an approximately north–south orientation, and one in the northeast part, exhibiting an approximately east–west direction, are visible.

We use *SDO/AIA* 171 and 1600 Å images to pinpoint the location of the eruption of the three CMEs within the AR. CME1 erupted in the southeast part of the AR, as indicated by the development of flare ribbons (visible in 1600 Å, Figure 1(d)) and by the southward expansion of coronal loops during the eruption (visible in 171 Å, not shown here). A posteruptive arcade (PEA) (visible in Figure 1(j)) also formed after the first eruption until the onset of the second eruption. Starting at 20:28 UT, associated with the eruption of CME2, more extended flare ribbons developed in the northern part of the AR (Figure 1(e)). These observations suggest that the eruption of CME1 remained confined to the southeast part of the AR, while the eruption of CME2 developed through the whole PIL system up to its northwest end (Figure 1(b)). The formation of a stable PEA is visible in the AIA 193 Å filter (Figure 1(k)), confirming that the magnetic reconnection processes associated with the eruption extended over the whole PIL system elongation. The short waiting time between CME1 and CME2 (less than 3 hr) and their origin from the same AR strongly favor the scenario of quasi-homologous CMEs, where the second eruption is commonly interpreted as a consequence of the flux rope destabilization caused by the rearrangement of coronal magnetic fields following the first eruption (Török et al. 2011; Bemporad et al. 2012; Chatterjee & Fan 2013; Wang et al. 2013; Liu et al. 2017). The eruption of CME3, occurring about 41 hr after CME2, originated from the vertical PIL located around the center of the AR, where changes in the surface magnetic field in 45 s HMI observations are visible starting from 11:54 UT (see also Mitra et al. 2018). Bright flare ribbons visible in the AIA 1600 Å line (Figure 1(f)) and a PEA visible in the AIA 193 Å filter (Figure 1(l)) indicate that magnetic reconnection extended over the whole PIL elongation (Figure 1(c)).

## 2.3. In Situ Observations at Earth

Figure 2 shows 1 minute averaged in situ measurements taken by the *Wind* and *DSCOVR* spacecraft during the days following the eruptions, together with the 1 hr Dst index measured on ground (provided by the World Data Center for Geomagnetism, Kyoto; <http://wdc.kugi.kyoto-u.ac.jp/dstdir/>).

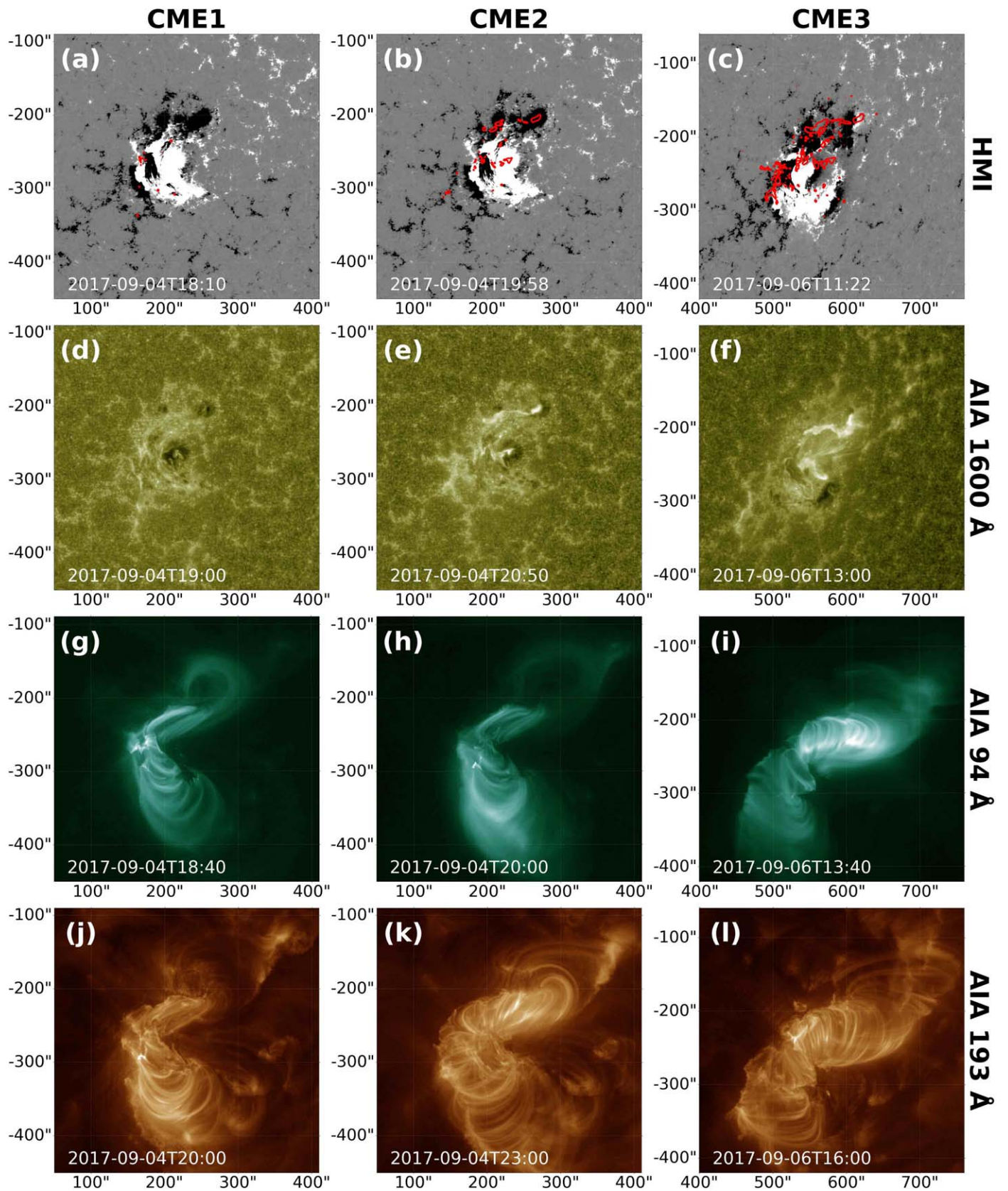


**Figure 1.** *SDO* observations of AR 12673 around the eruption times of the CMEs under study. ((a)–(c), top row) *SDO*/HMI line-of-sight magnetograms with red contours indicating the location of flare ribbons from *SDO*/AIA images in the 1600 Å filter ((d)–(f), second row). ((g)–(i), third row) *SDO*/AIA images in the 94 Å filter. ((j)–(l), bottom row) *SDO*/AIA images in the 193 Å filter.

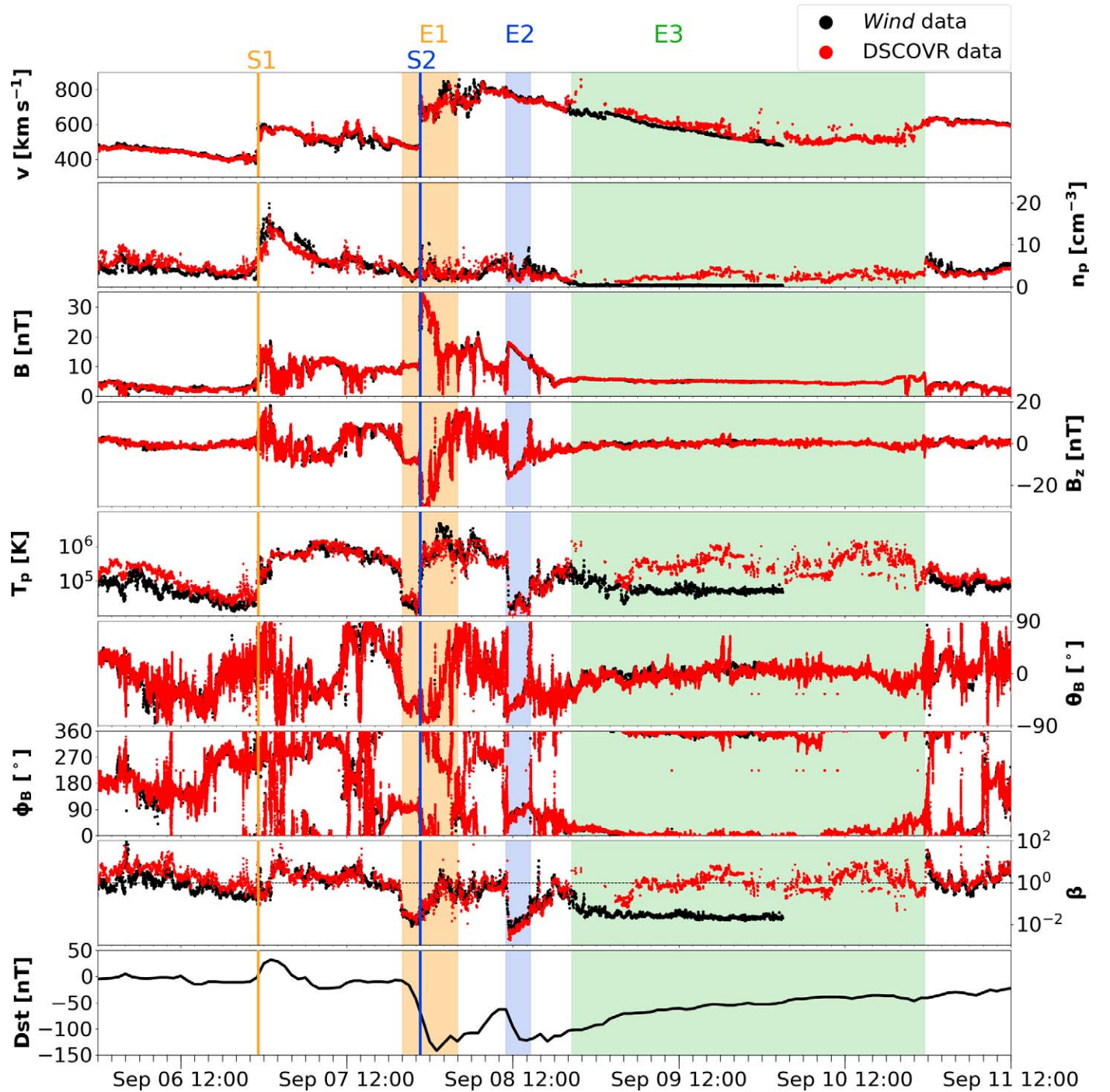


**Figure 2.** 1 minute averaged solar wind magnetic field and plasma parameters from the *Wind* (in black) and *DSCOVR* (in red) spacecraft at L1, between 2017 September 6 and 11. From top to bottom: plasma speed ( $v$ ), proton number density ( $n_p$ ), magnetic field magnitude ( $B$ ), magnetic field  $B_z$  component in geocentric solar ecliptic (GSE) coordinates, proton temperature ( $T_p$ ), magnetic field elevation ( $\theta_B$ ), magnetic field azimuthal angle ( $\phi_B$ ), proton plasma  $\beta$ . The bottom panel shows the 1 hr Dst index. The vertical lines mark the interplanetary shocks S1 and S2, and the shaded areas mark the periods associated with magnetic ejecta E1, E2, and E3.

Since CME1 and CME2 are observed to merge into a single structure (hereafter CME1+CME2) in the fields of view of LASCO and SECCHI, that is, already in the corona, it is reasonable to expect them to drive a single, common shock (e.g., Odstreil et al. 2003; Xiong et al. 2007; Lugaz et al. 2013) as they propagate in interplanetary space, most probably the one observed at *Wind* at 23:13 UT on September 6 (hereafter S1). S1 was followed by a prolonged sheath region (with a duration of  $\sim 21$  hr, corresponding to a thickness of  $\sim 0.25$  au

for a structure moving at  $\sim 500$  km s<sup>-1</sup>) characterized by a fluctuating magnetic field and relatively high density and temperature. Such a structure can imply a spacecraft crossing through a thick sheath region formed by the merging of the CME1 and CME2 sheaths, whose formation is compatible with the early merging of the two CMEs. On September 7 around 20:00 UT a region of low plasma  $\beta$  and smooth magnetic field, compatible with a magnetic ejecta (hereafter E1), was observed. E1, most probably associated with the merged

CME1+CME2 ejecta, was also listed in the Richardson & Cane list of interplanetary CMEs (<http://www.srl.caltech.edu/ACE/ASC/DATA/level3/icmetable2.htm>; Cane & Richardson 2003; Richardson & Cane 2010) with start time around 20:00 UT and end time around 04:00 UT on September 8, that is, with a duration of 8 hr. In the list, the ejecta was classified with a quality flag equal to 1, indicating that it exhibited only some of the typical characteristics of magnetic clouds, for example, a low plasma  $\beta$  and coherent magnetic field rotation, but lacked some other characteristics such as an enhanced magnetic field magnitude.

Moreover, the ejecta was characterized by the presence of an interplanetary shock (hereafter S2) propagating through it. The shock was observed at 22:38 UT on September 7, that is, 2.5 hr after the start of E1, and it was most likely driven by CME3. S2 compressed the magnetic field of the E1 ejecta, resulting in a significant amplification of the southward  $B_z$  from a preexisting value of  $\sim -10$ , to  $\sim -30$  nT. The negative  $z$ -component of the magnetic field in the shock upstream region triggered the beginning of a geomagnetic disturbance, marked by a decrease in the Dst index to about  $-50$  nT. The further enhancement of the negative  $B_z$  in the downstream region led to the development of the first and strongest dip in the Dst profile, reaching  $-142$  nT around 1 UT on September 8. Overall S2 presented several characteristics typical of shocks propagating inside preceding ejecta, including a low  $\beta$  in the upstream and downstream shock regions, and a magnetic field clock angle almost constant across the shock (Lugaz et al. 2015, 2017).

A second period of enhanced magnetic field and low  $\beta$  was observed between 11:00 UT on September 8 and 20:00 UT on September 10. This period was classified in the Richardson & Cane ICME list as a single ejecta with a quality flag equal to 1. However, we note the presence of a region of fluctuating fields and relatively high proton temperature and plasma  $\beta$  between 14:30 UT and 20:30 UT on September 8, which suggests the passage of two separate ejecta regions (hereafter E2 and E3). Both E2 and E3 exhibited low plasma  $\beta$  and enhanced magnetic fields with different levels of rotation. The period marked as E2 is characterized by a rotating magnetic field, a typical characteristic of spacecraft crossings through the flux rope structure. This ejecta period is most probably associated with the passage of CME3 that also drove S2. E3 exhibits typical characteristics of leg encounters, as featured by the large  $B_x$  component (not shown), the lack of magnetic field rotations, and a long duration (Marubashi & Lepping 2007; Möstl et al. 2010; Kilpua et al. 2011, 2013; Owens 2016). In view of the coronal and in situ CME/ICME observations, we consider it most probable that E2 and E3 were associated with the same CME (i.e., CME3) at the Sun and simply corresponded to crossings of the spacecraft through different parts of the flux rope. In this picture, E2 would correspond to a passage closer to the apex of CME3 and E3 to the passage through its leg. Additional evidence is provided by the speed profile, which decreases very coherently through and between E2 and E3, as well as by the coherent rotation of the magnetic field vectors. This interpretation would require a bending or deformation of the flux rope global structure as a consequence of its interaction with the ambient solar wind or preceding ejecta (Crooker et al. 1998; Mulligan et al. 1999; Dasso et al. 2007; Marubashi & Lepping 2007). The passage of E2 generated a second dip in the Dst index (minimum of  $-124$  nT on September 8 around 13 UT), that is, the complex

ejecta investigated here resulted in a two-step geomagnetic storm (Farrugia et al. 2006; Liu et al. 2014b). The magnetic field in E3 was low (about 5 nT) and pointed primarily to the north. As a consequence, the Dst recovered during E3 without further intensification.

We note that in such high-activity periods, the identification of ICME signatures and their linking with the corresponding CMEs at the Sun become very complex due to interactions among the various structures in the corona and interplanetary space and the elevated number of potential CME candidates. For this reason, we cannot rule out a priori that E2 and E3 were associated with two different CMEs at the Sun, possibly involving the faint partial halo CME discussed in Section 2.1. However, in order to keep the assumptions as simple as possible at the beginning, in our simulations we consider both ejecta to be associated with CME3. This is a reasonable assumption as our primary focus concerns the investigation of the nature and evolution of the main geoeffective structures, that is, the southward field in E1 due to the compression by S2 and the southward field in E2, rather than the origin of E3. We also note that with this interpretation our in situ analysis is consistent with the previous studies by Shen et al. (2018) and Werner et al. (2019).

Between the end of E1 and the start of E2, a region characterized by plasma  $\beta \sim 1$ , modest and fluctuating magnetic fields, and increasing density suggests the occurrence of magnetic reconnection at the interaction surface between E1 and E2 (Maričić et al. 2014). These in situ signatures exhibit several characteristics of ongoing CME–CME interactions, consistent with a picture in which the interaction of CME1+CME2 and CME3 was still at an early stage at 1 au (Lugaz et al. 2015, 2017).

### 3. Methods and Models

#### 3.1. CME Kinematics and Geometry

During the days of the CME eruptions, *STEREO-A* was located at a longitude of  $-128^\circ$  in Stonyhurst coordinates (Thompson 2006), providing a second vantage point to investigate the coronal evolution of the CMEs under study, in addition to the observations made along the Sun–Earth line. To constrain the kinematics and geometry of the CMEs in the corona, we perform a 3D fitting of the events from these two viewpoints (*SOHO* and *STEREO-A*) using the graduated cylindrical shell (GCS; Thernisien et al. 2006, 2009) model. The results from the GCS fitting are then used as input for the CME modeling using EUHFORIA (Section 3.3).

The GCS fitting provides as output the following parameters (in Stonyhurst coordinates): CME latitude ( $\theta_{\text{CME}}$ ), longitude ( $\phi_{\text{CME}}$ ), front height ( $h_{\text{CME}}$ ), aspect ratio ( $\kappa_{\text{CME}}$ ), half angle ( $\alpha_{\text{CME}}$ ), and tilt ( $\gamma_{\text{CME}}$ ). For  $\alpha_{\text{CME}} \neq 0^\circ$ , the shell of the GCS model corresponds to a croissant-like shape. From the aspect ratio and half angle we derive the edge-on (EO), face-on (FO), and average (AV) CME half-widths ( $\omega_{\text{CME}}/2$ ) (Thernisien et al. 2009). From a modeling perspective, the determination of a single value for the CME half-width from raw GCS outputs is critical because in EUHFORIA CMEs are initialized with spherical shapes, that is, their cross sections are symmetric in all directions. From the fitting of sequential images, we also derive the deprojected (3D) speed of the CME apex ( $v_{\text{CME}}$ ) as well as the radial/translational CME speed ( $v_{\text{CME}}^{\text{rad}}$ , corresponding to the speed of the center of the croissant tube) and the CME expansion speed ( $v_{\text{CME}}^{\text{exp}}$ , corresponding to the rate of increase of the croissant cross-sectional radius) (Scolini et al. 2019,

**Table 1**  
Results from the GCS Fitting of the Three CMEs under Study

Parameter	CME1	CME2	CME3
$\theta_{\text{CME}}$	0°	-25°	-11°
$\phi_{\text{CME}}$	25°	0°	21°
$\kappa_{\text{CME}}$	0.38	0.50	0.43
$\alpha_{\text{CME}}$	10°	30°	15°
$\omega_{\text{CME}}/2$ (EO/ AV/FO)	22°/27°/32°	30°/45°/60°	25°/33°/40°
$\gamma_{\text{CME}}$	0°	0°	40°
$v_{\text{CME}}$	960 km s <sup>-1</sup>	1585 km s <sup>-1</sup>	1910 km s <sup>-1</sup>
$v_{\text{CME}}^{\text{rad}}$	697 km s <sup>-1</sup>	1057 km s <sup>-1</sup>	1293 km s <sup>-1</sup>
$v_{\text{CME}}^{\text{exp}}$	263 km s <sup>-1</sup>	528 km s <sup>-1</sup>	617 km s <sup>-1</sup>
Time at 0.1 au	2017 Sep 4 23:00 UT	2017 Sep 4 22:44 UT	2017 Sep 6 14:11 UT

**Note.** EO = edge-on, FO = face-on, AV = average.

see also Appendix A for the analytical derivation). Each speed was determined by performing a linear fitting of instantaneous results from LASCO/C2–C3 and STEREO/COR2-A images (CME1: between 19:54 UT and 20:39 UT on September 4, for a total of three images; CME2: between 20:39 UT and 21:54 UT on September 4, for a total of five images; CME3: between 12:39 UT and 13:54 UT on September 6, for a total of five images).

Table 1 lists the results of the GCS fitting for the three events under study. Snapshots of the GCS fitting results overplotted on LASCO/C3 and STEREO/COR2-A images are provided in Appendix A. We note that from the extrapolation of the times at which the CME leading edges reached 0.1 au, we ascertain that CME2 reached this distance about 15 minutes earlier than CME1. This indicates that the interaction between CME1 and CME2 occurred at heliocentric distances close to or slightly lower than 0.1 au.

### 3.2. CME Magnetic Parameters

In preparation for the heliospheric CME simulations with the spheromak flux rope model in EUHFORIA (discussed in Section 3.3), we discuss in the following subsections the observational derivation of three key parameters characterizing the magnetic (flux rope) structure of the CMEs under study: their chirality, tilt, and the amount of magnetic flux reconnected during the eruption.

#### 3.2.1. Chirality and Tilt of the Flux Ropes

*Chirality of the Flux Ropes*—Observationally, the magnetic helicity sign (or *chirality*) of ARs can be inferred from different morphological features (e.g., Démoulin & Pariat 2009; Palmerio et al. 2017). In the particular case under study, images in the extreme-ultraviolet SDO/AIA filter at 94 Å (Figures 1(g)–(i)) suggest that AR 12673 was characterized by a negative chirality as indicated by the presence of a reverse-S sigmoid in its northern part, which is also consistent with the recent analyses by Mitra et al. (2018), Yan et al. (2018), and Price et al. (2019). Although cases of inconsistency between the chirality of the source region and that of the erupted CME have been observed (e.g., Chandra et al. 2010), for most of the events the two are found to match (Bothmer & Schwenn 1998; Palmerio et al. 2018). For this reason, in the following analysis

we start by assuming the erupted structures are characterized by a negative chirality as their source region.

*Tilt of the Flux Ropes*—In order to estimate the orientation of the flux ropes at the Sun, we use proxies based on the orientation of PEAs and PILs (Möstl et al. 2008; Palmerio et al. 2017, 2018). As shown in Figure 1, the PEA forming after the eruption of CME1 was confined to the southern portion of the AR/PIL and exhibited an approximately north–south orientation. For CME2 and CME3, we observe PEAs developing along the whole PIL structure. Although a global direction from southeast to northwest can be identified, the shape of such PEAs appears to be bent in a reverse-S shape. This reflects the complexity of the underlying PIL system and makes the determination of an unambiguous flux rope tilt based on such observations extremely difficult. Similar conclusions about the initial flux rope tilts can be obtained by considering the locations of coronal dimmings and flare ribbons (Figure 3). Combining these tilts with the information about flux rope chirality and magnetic polarity regions from HMI magnetograms, we recover an ENW flux rope type for CME1 and intermediate ENW–NWS flux rope types for CME2 and CME3 in the lower corona (using the same classification as Bothmer & Schwenn 1998; Mulligan et al. 1998; Palmerio et al. 2018).

To constrain the orientation of the flux ropes in the upper corona ( $\sim 5 R_{\odot}$  to  $\sim 20 R_{\odot}$ ), we consider the results from the GCS fittings. The derived tilts suggest that the axial magnetic field of CME1 and CME2 is oriented parallel to the solar equatorial plane ( $\gamma_{\text{CME}} = 0^\circ$ ), while that of CME3 has an inclination of  $\sim 40^\circ$  with respect to the solar equator. According to reconstruction of the heliospheric current sheet (HCS) by potential-field source-surface (Altschuler & Newkirk 1969) models (from the Global Oscillation Network Group (GONG): <https://gong.nso.edu/data/magmap/pfss.html>), the derived CME tilts are (quasi-) aligned to the HCS (Yurchyshyn 2008; Isavnin et al. 2014). Using the GCS tilt estimates as given in Table 1 and assuming the flux rope chirality at the source region to be preserved in spacetime, two possible flux rope types are possible for each CME. CME1 and CME2 are most probably either SEN flux rope types or NWS flux rope types. CME3 can be associated either with an intermediate ENW–NWS flux rope or with an intermediate WSE–SEN flux rope. We note, however, that the  $\gamma_{\text{CME}}$  parameter is associated with the highest uncertainties (Thernisien et al. 2009), and it is known to be very sensitive to the subjectivity involved in performing the GCS fitting (see, e.g., Figure 5 in Shen et al. 2018, for an alternative fitting of the CMEs using the GCS model, leading to a quite different interpretation of the tilt angles in the corona). For this reason, we consider its reconstruction particularly uncertain.

Overall, the comparison of the CME flux rope types recovered in the lower and upper corona suggests that CME1 and CME2 underwent considerable rotations (rotation  $\geq 90^\circ$  for CME1,  $\geq 45^\circ$  for CME2, and  $\geq 0^\circ$  for CME3). Similar conclusions are reached when considering the GCS fitting performed by Shen et al. (2018). Such estimates are in the upper range of reported values (Lynch et al. 2009; Vourlidis et al. 2011; Isavnin et al. 2014; Kay et al. 2015) but are not surprising given the sympathetic nature of CME1 and CME2, consistent with a scenario of early interactions and strong magnetic forces that may have led to significant CME rotations (Kay et al. 2015).

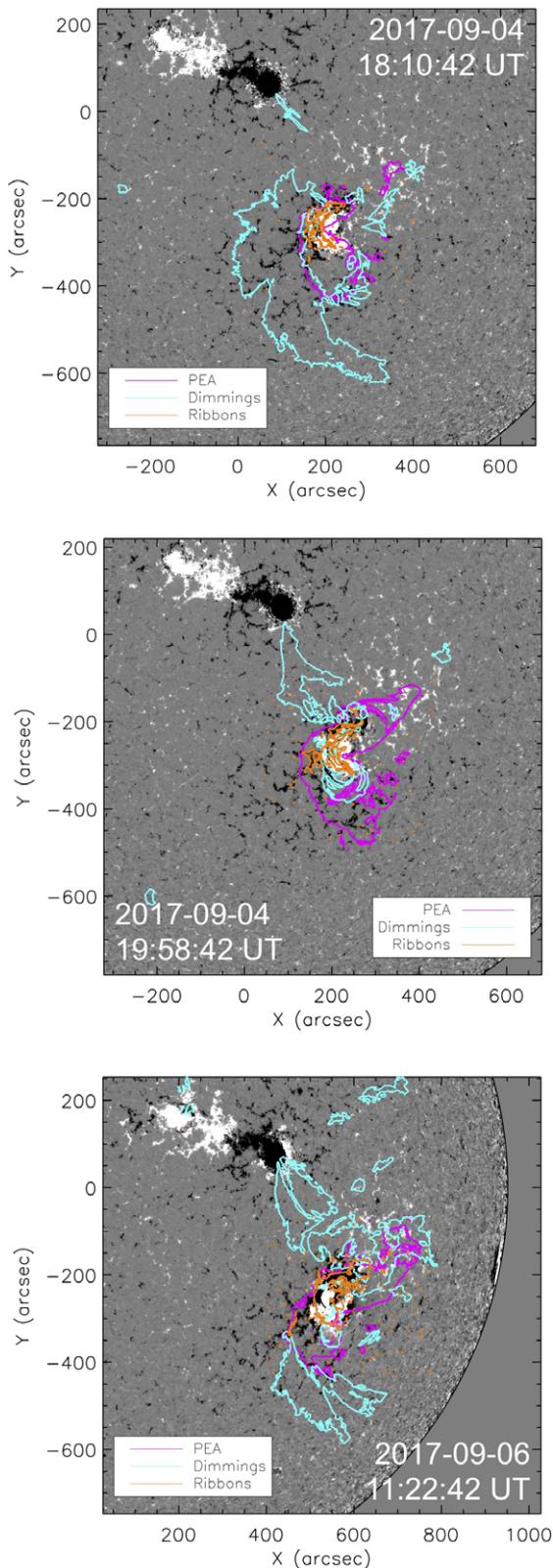


**Figure 3.** Location of flare ribbons (orange curves), coronal dimmings (cyan curves), and PEAs (magenta curves) associated with the eruption of CME1 (top), CME2 (middle), and CME3 (bottom). The gray-scale backgrounds show the HMI line-of-sight magnetic fields on September 4 at 18:16 UT (top) and 19:58 UT (middle) and September 6 at 11:23 UT (bottom), saturated to  $\pm 100$  G, with black and white representing the negative and positive polarities, respectively.

*Association with Interplanetary Structures*—In order to further confirm the associations between the CMEs and their interplanetary counterparts described in Section 2.3, we also compare the helicity sign and the flux rope types of the corresponding ejecta at the Sun with the magnetic structures recovered in situ.

The magnetic field rotations observed in association with E1 (most probably associated with the structure resulting from the merging of CME1 and CME2) indicate that the ejecta can be described as a left-handed flux rope characterized by a  $\sim 45^\circ$  inclination between an SEN- and an ENW-type at 1 au, although the presence of shock S2 propagating through E1 makes the interpretation of the flux rope type particularly problematic because of the disturbed properties in the downstream region. The magnetic field rotations within E2 indicate that the second ejecta can be described as a left-handed low-inclination flux rope of SEN type at 1 au. The lack of magnetic field rotations within E3 makes it difficult to determine the flux rope type of this structure. Overall, the chiralities of the flux ropes recovered from in situ observation at Earth are consistent with the chiralities recovered from source region images. On the other hand, occurrence of significant rotations in the corona and/or interplanetary space is needed to explain the different flux rope orientations recovered at the source region, in the upper corona, and at 1 au. Although deviating from typical scenarios, this aspect can be interpreted as a consequence of the multiple coronal and interplanetary interactions that occurred among the CMEs under study, as well as with other heliospheric structures (e.g., the HCS).

### 3.2.2. Reconnected Magnetic Fluxes

In order to perform EUHFORIA simulations with the spheromak CME model, next to observational estimations of the flux rope tilts and chiralities, we also need an estimate of the amount of magnetic flux contained within the magnetic structure. As a proxy, we use the flux ( $\varphi_r$ ) that reconnected in association with each CME eruption. To have a robust estimate of  $\varphi_r$ , we compare the results obtained from the analysis of a variety of posteruptive signatures (such as flare ribbons, coronal dimmings, and PEAs) in the AR involved in the eruptions.

*Statistical Relations*—We first estimate the reconnected fluxes using CME–flare statistical relations proposed in previous works. Among all, we focus on the relations between the flare peak intensity in soft X-rays and the reconnected flux derived from flare ribbons and coronal dimmings (e.g., Kazachenko et al. 2017; Dissauer et al. 2018a; Tschernitz et al. 2018) and on the relations between the CME speed and the reconnected flux derived from PEAs (Pal et al. 2018). The major advantages in using statistical relations instead of an in-depth analysis of single events are the applicability to a larger set of events (not restricted to eruptions originating close to the disk center and characterized by specific posteruptive signatures) and the simplicity of use, which makes them potentially suitable for operational forecasting applications, as they can be used to routinely initialize the parameters used by physics-based flux rope CME models running in forecasting mode.

Tschernitz et al. (2018) studied a set of 51 flares ranging between B3 and X17 in *GOES* class, reporting a very tight correlation (Pearson correlation coefficient  $r_p = 0.92$  in log–log space) between the flare peak intensity  $I_{\text{SXR}}$  (in units of

$\text{W m}^{-2}$ ) and the reconnected flux  $\varphi_r$  (in units of Mx) estimated from flare ribbons:

$$\log(\varphi_r) = 24.21 + 0.58 \log(I_{\text{SXR}}). \quad (1)$$

Considering a larger sample of about 3000 flares ranging from C1 to X5 in *GOES* class (RibbonDB catalog, <http://solarmuri.ssl.berkeley.edu/~kazachenko/RibbonDB/>), Kazachenko et al. (2017) reported a correlation of

$$\log(\varphi_r) = 24.72 + 0.64 \log(I_{\text{SXR}}), \quad (2)$$

with Spearman's rank correlation coefficient  $r_s = 0.66$ . Correcting for the different definitions of  $\varphi_r$  used by Kazachenko et al. (2017) ( $\varphi_r = \text{total (unsigned) magnetic flux}$ ) compared with Tschernitz et al. (2018) ( $\varphi_r = \text{average of the positive and negative fluxes}$ ), the relation in Equation (2) becomes

$$\log(\varphi_r) = 24.42 + 0.64 \log(I_{\text{SXR}}), \quad (3)$$

where  $\varphi_r$  is now defined to be consistent with the definition used by Tschernitz et al. (2018). Considering the large span of the flare *GOES* classes associated with the three CMEs under study (M1.7 to X9.3) and the higher correlation coefficients reported by Tschernitz et al. (2018) and Kazachenko et al. (2017) compared with other studies, in the following we use Equations (1) and (3) to identify the most probable range of flare ribbon reconnected flux values  $\varphi_r$  associated with each CME event.

In addition to flare ribbons, we consider coronal dimmings as a secondary signature to estimate the reconnected flux during the eruptions under study based on flare peak intensities. Dissauer et al. (2018a) performed a statistical analysis based on coronal dimming regions observed in association with a set of 62 CME events, reporting a correlation between the flare peak intensity and reconnected flux estimated from coronal dimmings equal to

$$\log(\varphi_r) = 23.26 + 0.42 \log(I_{\text{SXR}}), \quad (4)$$

with  $r_p = 0.62$  (in log–log space).

Applying Equations (1), (3), and (4) to the flare peak intensities observed in association with the three CME events under study (obtained from the NOAA SWPC data archive, <ftp.swpc.noaa.gov/pub/warehouse>), that is,  $I_{\text{SXR}} = 1.7 \times 10^{-5} \text{ W m}^{-2}$  (CME1),  $I_{\text{SXR}} = 5.5 \times 10^{-5} \text{ W m}^{-2}$  (CME2), and  $I_{\text{SXR}} = 9.3 \times 10^{-4} \text{ W m}^{-2}$  (CME3), we obtain an estimate of the reconnected fluxes based on statistical relations as listed in Figure 4.

In a recent study, Pal et al. (2018) derived statistical relations linking the reconnected fluxes obtained from the Flux Rope from Eruption Data (FRED; Gopalswamy et al. 2017) method, using PEAs as a primary signature to calculate the reconnected flux, and the CME 3D speed  $v_{3D}$  (in units of  $\text{km s}^{-1}$ ) in the corona estimated by applying the GCS fitting technique. Based on 33 CME events, they reported a correlation of ( $r_p = 0.66$ )

$$v_{3D} = 327 \varphi_r^{0.69}. \quad (5)$$

Inverted, the relation above is

$$\varphi_r = \left( \frac{v_{3D}}{327} \right)^{1/0.69}, \quad (6)$$

which allows us to estimate the reconnected flux once the 3D speed of the CME is known. Using as input the 3D speeds reconstructed from the GCS fitting ( $v_{\text{CME}}$ ) listed in Table 1, the

reconnected fluxes for the three CMEs obtained from Equation (6) are provided in Figure 4.

*Reconnected Fluxes from Single-event Analysis*—In order to obtain an event-based estimate of the reconnected fluxes and to assess the performance of statistical relations in the specific case of the events considered, we complement the  $\varphi_r$  values recovered from statistical relations with results from the single-event analysis of each of the three eruptions under study. In order to consider a broad spectrum of CME-related signatures, we estimate the reconnected flux involved in each CME eruption using the following methods:

1. A method to identify flare ribbon areas based on the work by Kazachenko et al. (2017). Flare ribbons are detected in *SDO/AIA* 1600 Å images with 24 s cadence by applying a cutoff threshold based on the median image intensity. Images are taken between 30 minutes before and 3 hr after the start of the flare associated with each CME under study.
2. A method to identify coronal dimming areas based on the work by Dissauer et al. (2018b). Coronal dimmings are detected based on a thresholding method that is applied to logarithmic base ratio *SDO/AIA* 211 Å images. Similar to the flare ribbons, dimming pixels are detected between 30 minutes before the flare and up to 3 hr after the flare.
3. A method to identify PEA areas based on the FRED method described by Gopalswamy et al. (2017). For each CME under study, we use *SDO/AIA* 193 Å taken around the moment of maximal extension of the PEAs. We note that instead of performing a manual identification of the PEA areas as in Gopalswamy et al. (2017), we here employ an automatic identification algorithm using a cutoff threshold based on the median image intensity.

To recover  $\varphi_r$  based on the areas identified with the methods above, we use full-disk *SDO/HMI* line-of-sight magnetograms (`hmi.m_720s`) taken about 30 minutes before the flare start times (shown in Figure 3).

Results from the single-event analyses are listed in Figure 4, while the location of the various EUV signatures overplotted on HMI magnetograms for the three events is shown in Figure 3. The large spread in the recovered  $\varphi_r$  values from single-event analyses reflects the different areas covered by the signatures considered (ribbons, dimmings, and PEAs), and we note that large uncertainties affect the estimation of  $\varphi_r$ , that is, up to  $\pm 50\%$  of the measured value, as reported by various studies (Qiu et al. 2007; Gopalswamy et al. 2017; Pal et al. 2017; Temmer et al. 2017; Dissauer et al. 2018a; Tschernitz et al. 2018). Despite the scatter, the different values recovered can therefore be considered consistent within the (large) error bars. At the same time, these results highlight that when using this methodology one should aim to recover an order of magnitude for the reconnected flux, rather than a precise estimate of it.

When averaging out the variability of the  $\varphi_r$  results obtained from the different methods, we recover very similar results between the single-event analyses and the statistical analyses of CME1 and CME2 (rows in bold in Figure 4). The results from the two approaches for CME3, on the other hand, appear somehow less consistent. We note that a contributing factor to this variability comes from the fact that the CME erupted about  $40^\circ$  away from the solar disk center, which is close to the limit of the applicability of the single-event analysis methods due to the increased projection effects when

Parameter	CME1	CME2	CME3	
$\varphi_r$ (based on Kazachenko et al. 2017)	2.3	4.9	30	} statistical
$\varphi_r$ (based on Tschernitz et al. 2018)	2.8	5.5	28	
$\varphi_r$ (based on Dissauer et al. 2018a)	1.9	3.1	9.9	
$\varphi_r$ (based on Pal et al. 2018)	4.8	9.9	13	
$\varphi_r$ (average)	3.0	5.9	17	
$\varphi_r$ (based on Kazachenko et al. 2017)	0.81	0.78	3.9	} single-event
$\varphi_r$ (based on Dissauer et al. 2018a)	4.9	3.4	7.6	
$\varphi_r$ (based on Gopalswamy et al. 2017)	8.2	8.7	10	
$\varphi_r$ (average)	4.6	4.3	7.2	

**Figure 4.**  $\varphi_r$  (in units of  $10^{21}$  Mx) for the three CMEs under study as recovered from statistical and single-event analyses.

moving away from the disk center (e.g., Gopalswamy et al. 2017; Dissauer et al. 2018b). This most probably resulted in higher uncertainties affecting the reconstruction of  $\varphi_r$ , that is, the results from single-event and statistical analyses are still consistent among each other due to the larger error bars. Overall, these results indicate that for the specific events considered, using different statistical methods to quantify the reconnected fluxes provides results that are on average consistent with those of more sophisticated single-event analysis methods. Such statistical methods are fast and easy to apply as they only require as input easy to use data products, such as the peak intensity of the CME-associated flares or the 3D speed of the CME in the corona as recovered from the GCS fitting or other reconstruction methods. In the context of operational forecasting operations, these results therefore highlight how statistical methods could represent promising potential alternatives to otherwise time-consuming single-event analysis methods.

### 3.3. The EUHFORIA Model

Magnetohydrodynamic (MHD) simulations of the evolution of magnetized CMEs in the heliosphere are powerful complementary tools to observations, as they can provide information on the evolution of CME structures in 3D space that is often difficult to infer from remote sensing or in situ observational data alone—particularly in cases limited by single-spacecraft in situ measurements as here. In this work, we investigate the heliospheric propagation and interaction of the three successive CMEs under study using the EUHFORIA model.

EUHFORIA is a recently developed 3D MHD model of the inner heliosphere (Pomoell & Poedts 2018) that allows the modeling of the background solar wind and CME events using a linear force-free spheromak flux rope model (Verbeke et al. 2019b). The model is composed of (1) a semiempirical Wang–Sheeley–Arge-like (Arge et al. 2004) global coronal model that provides the background solar wind parameters at the heliocentric radial distance of 0.1 au, starting from synoptic maps of the photospheric magnetic field and (2) a time-dependent 3D MHD model of the inner heliosphere (between 0.1 and 2 au). In the heliosphere, it is possible to model solely the ambient solar wind or to also include CMEs, which are inserted into the heliospheric domain via time-dependent boundary conditions at 0.1 au. In this work we use a computational domain for the heliospheric model  $\pm 180^\circ$  in longitude ( $\phi$ ),  $\pm 80^\circ$  in latitude ( $\theta$ ), and from 0.1 to 2 au in the radial direction ( $D$ ). The use of a sufficiently high spatial resolution is particularly necessary to better resolve shock structures in the simulation domain, which are extremely important in the context of global CME–CME interactions, as discussed in Section 4. For this reason, our simulations are performed using a homogeneous grid with 1024 cells in the radial

direction (corresponding to a radial resolution of  $\Delta D = 0.00186$  au =  $0.4 R_\odot$  per cell) and with  $2^\circ$  resolution in the longitudinal and latitudinal directions. As input for the coronal model we use the magnetogram synoptic map generated by the GONG on 2017 September 4 at 00:04 UT ([https://gong.nso.edu/data/magmap/QR/bqs/201709/mrbqs170904/mrbqs170904t0004c2194\\_055.fits.gz](https://gong.nso.edu/data/magmap/QR/bqs/201709/mrbqs170904/mrbqs170904t0004c2194_055.fits.gz)). All simulations are carried out with EUHFORIA, version 1.0.4. In the following, all coordinates are given in the heliocentric earth equatorial coordinate system, unless specified otherwise.

#### 3.3.1. CME Modeling

In this work, we initialize spheromak CMEs at 0.1 au using the following observation-based parameters recovered from the GCS fitting: longitude ( $\theta_{\text{CME}}$ ), latitude ( $\phi_{\text{CME}}$ ), and half-width ( $\omega_{\text{CME}}/2$ , average of the values provided in Table 1). Moreover, the speeds of the inserted CMEs are set using the CME radial speed  $v_{\text{CME}}^{\text{rad}}$  derived from the GCS fitting, as discussed in detail by Scolini et al. (2019). Due to the more limited observational constraints available, two additional parameters, the CME mass density and temperature, are set to default values ( $\rho_{\text{CME}} = 10^{-18}$  kg m $^{-3}$  and  $T_{\text{CME}} = 0.8 \times 10^6$  K, respectively). The speed, density, and temperature are set to be homogeneous within the CME body during the insertion in the heliosphere. The three parameters that describe the magnetic structure of spheromak CMEs are partially derived from observations. The magnetic chirality is set equal to  $-1$  (negative, indicating a left-handed flux rope) for all CMEs, as provided by the low-coronal observations of the source region. Due to the large uncertainties affecting the reconstructed orientation ( $\gamma_{\text{CME}}$ ) of the CME magnetic structures at 0.1 au (i.e., because of observational limitations in white-light images, subjectivity in the GCS fitting, and strong CME rotations, as discussed in Section 3.2), we test several tilt angles  $\tau$  for the spheromak configurations in EUHFORIA. Among all of these, an initial tilt corresponding to a WSE flux rope type for all three CMEs provides the best  $B_z$  predictions compared with in situ observations. We set the toroidal magnetic flux  $\varphi_t$  of each spheromak CME based on the estimated reconnected flux  $\varphi_r$  derived from statistical and single-event studies (Figure 4, using the same methodology as Scolini et al. 2019) and under the assumption that the reconnected flux only contributes to the poloidal flux of the flux rope (i.e.,  $\varphi_r \approx \varphi_p$ ; Qiu et al. 2007; Möstl et al. 2008; Gopalswamy et al. 2017). The results (rounded to the closest integer) calculated from the  $\varphi_r$  estimates are  $\varphi_t = 5 \times 10^{21}$  Mx (CME1),  $\varphi_t = 5 \times 10^{21}$  Mx (CME2), and  $\varphi_t = 1 \times 10^{22}$  Mx (CME3).

We perform a total of five simulations, labeled according to the following format: “XX-XX-XX” is a generic simulation with “XX” being the label of individual CMEs. The label “00” means that a given CME is not modeled, while “01” means that the CME was modeled. We start by performing one simulation (run 00-00-00) without any CMEs inserted, in order to characterize the ambient solar wind through which the three CMEs propagated. We then perform a set of three runs where we progressively add one CME at a time in our simulations, that is, first modeling only CME1 (run 01-00-00), then including also CME2 (run 01-01-00), and finally adding CME3 (run 01-01-01). This is done to see how the modeling results change by consecutively adding CMEs in the simulations, in order to better isolate the contribution of each CME to the final modeling results and the effect of the CME–CME interactions on the propagation of CME1 and CME2. Finally, we also perform a simulation with CME3 alone

**Table 2**  
Summary of the EUHFORIA Simulations Performed in This Study

Run Number	CME1	CME2	CME3
00-00-00	–	–	–
01-00-00	spheromak	–	–
01-01-00	spheromak	spheromak	–
01-01-01	spheromak	spheromak	spheromak
00-00-01	–	–	spheromak

(run 00-00-01), which allows us to compare the propagation of CME3 with or without the presence of the preceding CMEs. The complete list of simulations is provided in Table 2. Full 3D simulations outputs of the whole heliospheric domain are extracted with a 1 hr cadence, while time series of all MHD variables at Earth and selected virtual spacecraft are produced with a 10 minute cadence. Similarly to Scolini et al. (2019), we place in our simulation domain an array of virtual spacecraft in the surroundings of Earth, separated by an angular distance of  $\Delta\sigma = 5^\circ$  and  $\Delta\sigma = 10^\circ$  (different combinations of longitudes and latitudes are considered), in order to assess the spatial variability of the results in the vicinity of Earth.

### 3.4. Geoeffectiveness Predictions and Dst Index

In order to quantify the resulting geoeffectiveness of the CME events as predicted by EUHFORIA, we calculate the predicted Dst index from the modeled time series at Earth after conversion into geocentric solar magnetospheric (GSM) coordinates, using the AK2 model proposed by O’Brien & McPherron (2000a, 2000b). Such predictions are compared with hourly Dst values from the World Data Center for Geomagnetism, Kyoto (<http://wdc.kugi.kyoto-u.ac.jp/dstdir/>), and with predictions obtained by applying the same coupling function to 1 minute solar wind time series provided by *Wind*.

The quality of the CME geoeffectiveness predictions is then quantified by comparing the minimum Dst predicted by EUHFORIA, with predictions obtained from *Wind* measurements and with actual observations.

## 4. Results and Discussion

In this section we present the results of the simulations performed, discussing the evolution of CME–CME interactions and their impact on the helio- and geoeffectiveness of individual CMEs.

### 4.1. Overview

An overview of the event in the heliosphere as obtained from EUHFORIA run 01-01-01 is presented in the top panels of Figure 5, showing the radial speed ( $v_r$ ) in the ecliptic plane and in the meridional plane containing Earth, at three different times in the simulation (the radial speed, number density, and colatitudinal magnetic field plots for all the runs performed are provided in Appendix B). The position of the leading edges of the CMEs as marked by their interplanetary shocks at various times are indicated by the black arrows. The bottom panel of Figure 5 shows the  $v_r$  prediction at Earth compared with in situ observations from *Wind* (a comparison of the EUHFORIA time series at and around Earth for all runs performed and in situ observations from *Wind* are included in Appendix C). The evolution and interactions of the CMEs in terms of 3D topology of their magnetic field lines, and of the plasma  $\beta$  and

$B_z (D/1 \text{ au})^2$  in the meridional plane containing Earth, are provided in Figure 6. The simulation results show that CME1 and CME2 interacted already during the insertion in the heliospheric domain, as expected given the very close insertion times derived from the GCS reconstruction (listed in Table 2) and from coronagraph images. In the heliosphere, the two CMEs propagate as a merged structure (hereafter CME1+CME2) all the way from 0.1 to 2 au. As further discussed in Section 4.3, its predicted arrival time at Earth supports the interpretation of S1 as the interplanetary shock driven by the CME1+CME2 merged structure. Figure 5 also shows CME3 first propagating through the perturbed solar wind in the wake of CME1+CME2 and then interacting with them. The interaction with CME1+CME2 appears to be still ongoing at the time CME3 reaches 1 au, as indicated by the shocks of CME1+CME2 and CME3 being still distinct as predicted at Earth, also supporting the interpretation of S2 being the interplanetary shock driven by CME3.

### 4.2. CME–CME Interactions in the Heliosphere

Because of the intrinsic difficulties in identifying the boundaries of the various ejecta and related structures in 3D, to characterize the phases of the interaction between CME1+CME2 and CME3 as they propagate in interplanetary space, we apply an approach based on 1D cuts taken along the Sun–Earth line (i.e., approximately the direction of propagation of the structures eventually arriving at Earth) at various times in our simulation (run 01-01-01). At each time, we identify the location of the leading and trailing shocks (driven by CME1+CME2 and CME3, respectively) and the boundaries of the two respective ejecta by considering a low- $\beta$  region to correspond to an ejecta. We also characterize the position of each ejecta in terms of their geometrical center. Figure 7 illustrates the main MHD parameters along the Sun–Earth line, together with the location of the various shock and ejecta structures, at three different times in the simulation, which clearly associate with three of the four typical phases of CME–CME interactions (as defined by Lugaz et al. 2005). In particular, Figure 7(a) associates with phase 1, corresponding to a period before the start of the interaction. Figure 7(b) associates with phase 2, corresponding to the shock–ejecta interaction phase, and Figure 7(c) with phase 3, corresponding to the shock–sheath interaction phase. Phase 4, corresponding to the shock–shock interaction phase, is not present in Figure 7 as this phase occurs after the CMEs have already left the simulation domain. A more detailed investigation of each interaction phase is given in the following paragraphs.

We also calculate the speed of the shocks and ejecta centers in the reference frame of the Sun. The propagation of each structure in terms of time–distance and time–speed profiles is shown in Figure 8.

At each time available, we characterize the properties of the trailing (CME3) shock by determining its speed in the reference frame moving with the upstream plasma by applying the Rankine–Hugoniot relations (assuming the 1D cut to be parallel to the shock normal) as

$$v_{\text{shock}} = \frac{v^{\text{down}} \rho^{\text{down}} - v^{\text{up}} \rho^{\text{up}}}{\rho^{\text{down}} - \rho^{\text{up}}}, \quad (7)$$

where “down” and “up” refer to quantities calculated in the downstream and upstream shock regions, respectively. In addition to the shock speed, we also calculate the Alfvén speed ( $v_A^{\text{up}}$ ), sound speed ( $c_s^{\text{up}}$ ), plasma  $\beta$  ( $\beta^{\text{up}}$ ) in the upstream region, and the shock Alfvén and magnetosonic (fast) Mach numbers

( $M_A$ ,  $M_{ms}$ ), together with the density compression ratio  $r = \rho^{\text{down}}/\rho^{\text{up}}$ . The evolution in spacetime of all these quantities is shown in Figures 9(a)–(e).

To clarify the relation between the evolution of the shock driven by CME3 and the evolution of the two ejecta, we also calculate the average scaled kinetic ( $\tilde{\epsilon}_{\text{kin}}$ ), magnetic ( $\tilde{\epsilon}_{\text{mag}}$ ), and thermal ( $\tilde{\epsilon}_{\text{therm}}$ ) energy densities within the two ejecta as

$$\begin{cases} \tilde{\epsilon}_{\text{kin}} = \langle \frac{1}{2} \tilde{\rho} \tilde{v}^2 \rangle \\ \tilde{\epsilon}_{\text{mag}} = \langle \frac{\tilde{B}^2}{2\mu_0} \rangle \\ \tilde{\epsilon}_{\text{therm}} = \langle \frac{2\tilde{n}k_B\tilde{T}}{\gamma - 1} \rangle \end{cases}, \quad (8)$$

where  $\gamma = 1.5$  is the adiabatic index (consistent with Pomoell & Poedts 2018),  $k_B$  is the Boltzmann constant,  $\langle x \rangle$  indicates the average along the radial coordinate taken over the ejecta extension calculated above, and  $\tilde{x}$  indicates a scaled quantity. Scaled quantities account for the radial evolution of the various CME parameters and are employed in order to better compare the energy densities at different times in the same run (corresponding to different distances from the Sun) and at the same times in different runs. This is needed because the propagation, that is, the radial distance, of the leading ejecta is greatly affected by the presence (run 01-01-01) or lack (run 01-01-00) of the interaction with CME3, and to compare its properties at the same time in the two runs, a correction for the different distance from the Sun is needed. In particular, we use the following scaling relations:  $\tilde{v} = v$ ,  $\tilde{n} = n (D/1 \text{ au})^{2.32}$ ,  $\tilde{\rho} = \rho (D/1 \text{ au})^{2.32}$ ,  $\tilde{B} = B (D/1 \text{ au})^{1.85}$ ,  $\tilde{T} = T (D/1 \text{ au})^{0.32}$ ,  $\tilde{P} = P (D/1 \text{ au})^{2.64}$ , with the exponents derived from statistical studies of CMEs in the inner heliosphere (from Liu et al. 2005; Gulisano et al. 2010). Together with the scaled energy densities, we also calculate the scaled radial size of the ejecta as  $\tilde{S} = S (D/1 \text{ au})^{0.45}$ , where the scaling factor is taken as the lower limit of the range obtained by Gulisano et al. (2010), which proves to scale well the decrease of the radial size of CME1+CME2 in the case without interaction (dashed red line in Figure 9(f)). We also apply the same approach to calculate the average energy densities in the region between the leading edge of the CME1+CME2 ejecta and its shock, corresponding to the sheath ahead of CME1+CME2. The evolution in time of the sizes and scaled energy densities associated with these three structures is shown in Figures 9(f)–(i).

Finally, we calculate the amplification of the helioeffectiveness of CME1+CME2 due to its interaction with CME3 in terms of the magnetic field compression caused by the propagation of the shock driven by CME3 through the CME1+CME2 ejecta. We therefore compute the maximum  $\tilde{B}$  ( $\tilde{B}^{\text{max}}$ ) and minimum  $\tilde{B}_z$  ( $\tilde{B}_z^{\text{min}}$ ) within the boundaries of the ejecta, where  $\tilde{B}_z = B_z (D/1 \text{ au})^{1.85}$  assuming that the magnetic field components in a CME scale with the same behavior as that of the magnitude  $B$ . The helioeffectiveness amplification factors ( $\tilde{A}$ ) due to the interaction are then calculated as  $\tilde{A}_B = \tilde{B}_{010101}^{\text{max}}/\tilde{B}_{010100}^{\text{max}}$  and  $\tilde{A}_{Bz} = \tilde{B}_{z,010101}^{\text{min}}/\tilde{B}_{z,010100}^{\text{min}}$ , that is, taking the ratio of the values from run 01-01-01 and run 01-01-00. Results are shown in Figure 9(j).

*Phase 1: Preinteraction*—In Figure 7(a), the shock and ejecta associated with CME3 propagate through a high- $\beta$  ( $\beta \sim 10$ ) solar wind perturbed by the earlier passage of the preceding CME1+CME2 structure. The rear edge of CME1+CME2 is still unaffected by the presence of CME3, indicating no direct interaction has yet occurred. This is also visible from the time–distance profile in Figure 8(a). At this time the shock driven by CME3 is propagating with a speed of  $\sim 2130 \text{ km s}^{-1}$  and its ejecta with a speed of  $\sim 650 \text{ km s}^{-1}$ , significantly higher than the shock and ejecta associated with CME1+CME2 (both moving at  $\sim 600 \text{ km s}^{-1}$ ). CME3 is progressively approaching CME1+CME2, as is clearly visible in Figure 8(a).

During this phase, the scaled energy densities of CME1+CME2 are approximately constant in spacetime (Figures 9(g)–(i)), implying that the (nonscaled) energy densities are decreasing with radial distance due to the known interplay of expansion (which converts magnetic and thermal energy into kinetic energy) and drag (which slows down the CME reducing its kinetic energy) (Cargill 2004; Vršnak et al. 2013). Between 18:00 UT and 21:00 UT on September 6, CME3 is still being inserted in the domain, and it expands (Figures 8(a), 9(f)) due to the propagation through the rarefied perturbed solar wind (Liu et al. 2014b; Temmer & Nitta 2015; Temmer et al. 2017), as indicated by its rapidly growing radial size and the rapid decrease of  $\tilde{\epsilon}_{\text{kin}}$ ,  $\tilde{\epsilon}_{\text{therm}}$ , and  $\tilde{\epsilon}_{\text{mag}}$  (Figures 9(g)–(i)).

*Phase 2: Shock–Ejecta Interaction*—On September 6 at 22:00 UT, around 0.45 au, the shock driven by CME3 starts interacting with the preceding CME1+CME2 ejecta (see Figures 7(b) and 8(a)). Figures 9(a)–(e) show that as the shock enters the preceding ejecta, the upstream plasma  $\beta$  decreases by a factor of 100, the upstream density decreases by a factor of 8, and the Alfvén speed increases by a factor of 12, while the sound speed remains almost the same. The reduced density and higher magnetic field contribute to increase  $v_A$  and to lower  $M_A$ ; hence the shock quickly accelerates from a speed of  $\sim 1300 \text{ km s}^{-1}$  to a speed of  $\sim 2120 \text{ km s}^{-1}$  on September 6 at 23:00 UT, while the density compression ratio of the shock decreases from  $r \simeq 5$  (with 5 equal to the theoretical maximum for ideal MHD with  $\gamma = 1.5$ ) to a value of about 1.9. After reaching the speed of  $\sim 2120 \text{ km s}^{-1}$ , the shock decelerates to a speed of  $\sim 970 \text{ km s}^{-1}$  when reaching the core (densest part) of the CME1+CME2 ejecta. The compression ratio is found to increase again to 2.9 a few hours later. The shock remains at all times a fast shock, with a minimum  $M_{ms}$  of 4.3 in the frame moving with the upstream plasma. Following the passage through the denser ejecta core, the shock propagates through a rarefied region where it accelerates up to  $\sim 2390 \text{ km s}^{-1}$  on September 7 at 10:00 UT, right before exiting the leading edge of the ejecta.

During this phase, the shock–ejecta interaction is most efficient in amplifying the helioeffectiveness of the CME1+CME2 ejecta, as is visible in the  $\tilde{A}_B$  and  $\tilde{A}_{Bz}$  amplification factors in Figure 9(j). The shock driven by CME3 compresses, accelerates, and heats the plasma in the preceding ejecta as it propagates through it, enhancing the density, speed, temperature, and magnetic field in the downstream region. This is visible as an increase in  $\tilde{\epsilon}_{\text{kin}}$ ,  $\tilde{\epsilon}_{\text{mag}}$ , and  $\tilde{\epsilon}_{\text{therm}}$  of CME1+CME2 compared with the simulation without interaction (i.e., red continuous and dashed lines in Figures 9(g)–(i)). The acceleration of CME1+CME2 is also clearly visible in the increased speed of the ejecta center in Figure 8(b). The radial size of CME1+CME2 also rapidly decreases (Figures 8(a) and 9(f)), consistent with a radial compression by the trailing shock

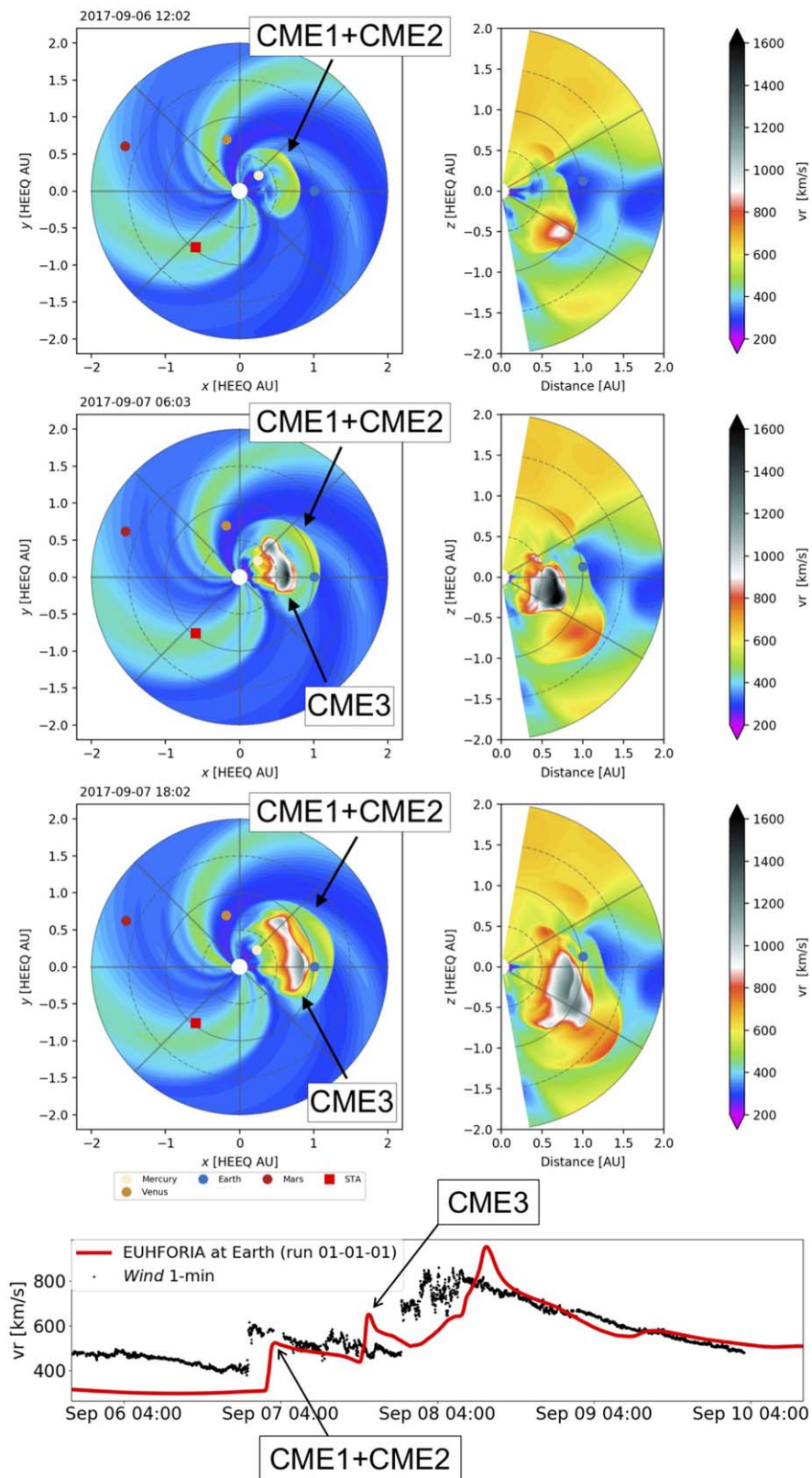


**Figure 5.** Top: propagation of the three CMEs in EUHFORIA simulations: snapshot of the radial speed  $v_r$ , from run 01-01-01 on 2017 September 6 at  $\sim$ 12:00 UT (top), 2017 September 7 at  $\sim$ 06:00 UT (middle), and 2017 September 7 at  $\sim$ 18:00 UT (bottom), in the heliographic equatorial plane (left) and in the meridional plane (right) that includes Earth (which is indicated by solid blue circles). The fronts of CME1, CME2, and CME3 are indicated by the black arrows. An animation of this figure is available. The animation runs from 00:03 UT on September 2 to 12:03 UT on September 10. Bottom: comparison of EUHFORIA time series (red) with in situ measurements from *Wind* (black).

(An animation of this figure is available.)

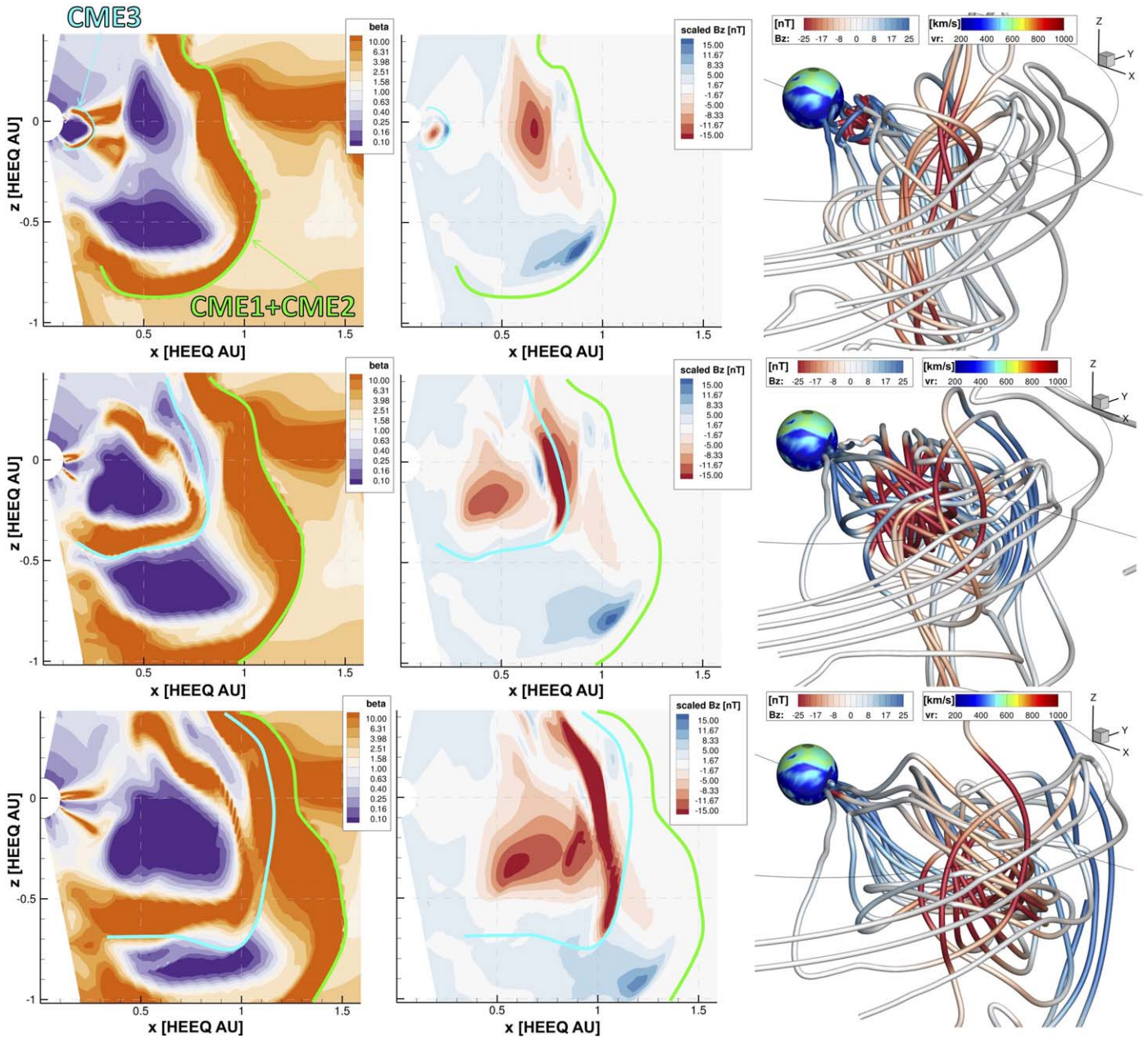


**Figure 6.** Interaction between CME1+CME2 and CME3 in EUHFORIA (run 01-01-01) at three different times: 2017 September 6 at 18:00 UT (top), 2017 September 7 at 06:00 UT (middle), and 2017 September 7 at 18:00 UT (bottom). Left: 2D view of the meridional plane containing Earth showing the different plasma  $\beta$  regions (purple:  $\beta < 1$ , marking magnetic ejecta; orange:  $\beta > 1$ , marking shock and sheath regions). The shocks associated with CME1+CME2 and CME3 are marked in green and cyan, respectively. Center: 2D view of the meridional plane containing Earth showing the scaled  $B_z$  ( $B_z(D/1 \text{ au})^2$ ) polarity regions (blue: marking positive, nonheliocffective regions; red: marking negative, heliocffective regions). Right: 3D view of the magnetic field lines in the heliospheric domain. The spherical contour shows the inner boundary ( $D = 0.1 \text{ au}$ ), colored based on the radial speed  $v_r$ . The magnetic field lines are colored based on  $B_z$ . The 1 au distance is marked by the black circle, the Sun–Earth line is marked by the black straight line, and the position of Earth is at the intersection of the two.

and ejecta (Vandas et al. 1997; Schmidt & Cargill 2004; Lugaz et al. 2005; Xiong et al. 2006). During this phase we observe a steady increase of the  $\tilde{A}_B$  and  $\tilde{A}_{B_z}$  amplification factors (“growth phase”), until maximum amplification factors of 3.3 for  $\tilde{A}_B$  and 2.8 for  $\tilde{A}_{B_z}$  are reached around September 7 at 14:00 UT, that is, after the end of this phase (“maximum phase”). The maximum heliocffective amplification occurs when the CME1+CME2 ejecta is around 0.9 au in simulation 01-01-01, that is, close to the location of Earth.

*Phase 3: Shock–Sheath Interaction*—Eventually, the shock driven by CME3 reaches the front of the CME1+CME2 ejecta

and starts interacting with the dense sheath of plasma ahead of it (Figures 7(c) and 8(a)). In our simulations, this occurs around September 7 at 11:00 UT, that is, close to the moment when it passes Earth/1 au. We note that this phase starts at smaller heliocentric distances than in the observed in situ data by the spacecraft at L1, where the shock appears still to be fully embedded in the ejecta. This is most probably due to a combination of two factors: (1) an overestimated drag in our simulations (lower speed and higher density in the solar wind ahead of CME1+CME2 compared with observations, see Appendix C)—this particularly contributed to slowing down

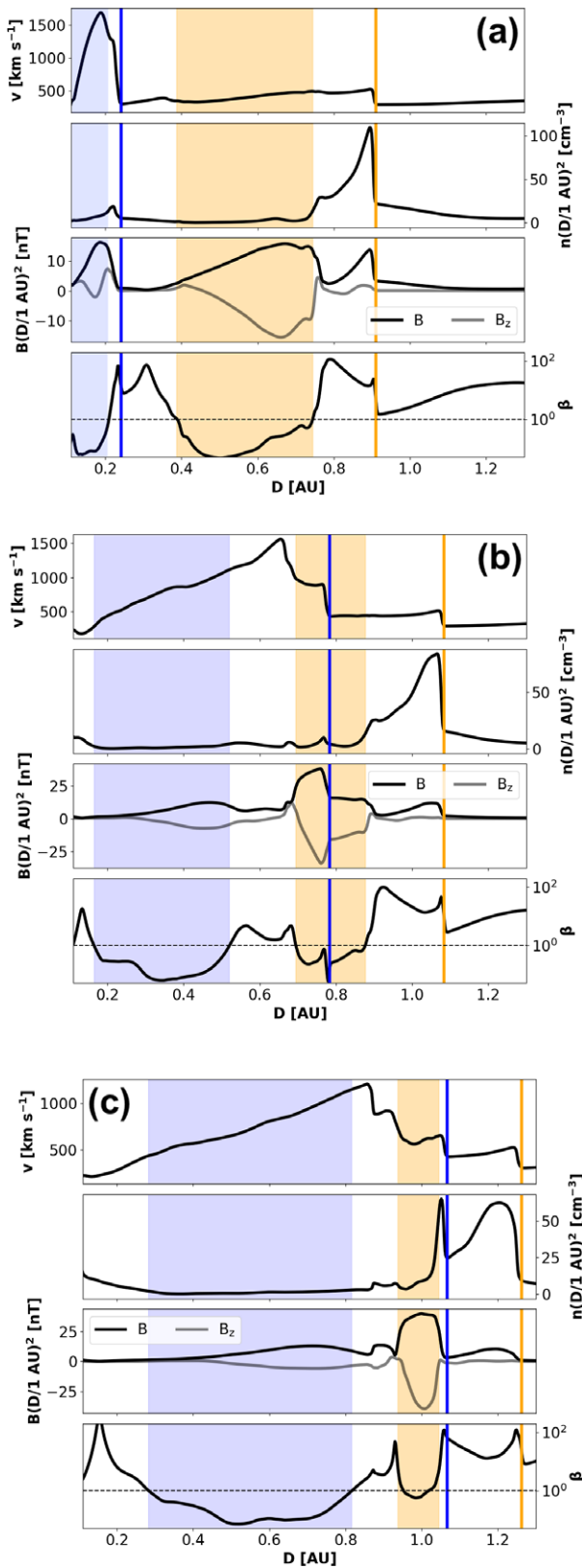


**Figure 7.** Interaction along the Sun–Earth line in EUHFORIA run 01-01-01, at the same times as in Figure 6. From top to bottom: speed ( $v$ ), scaled number density ( $n(D/1 \text{ au})^2$ ), scaled magnetic field magnitude ( $B(D/1 \text{ au})^2$ ) and north–south component ( $B_z(D/1 \text{ au})^2$ ), and plasma  $\beta$ . The orange and blue vertical lines indicate the location of the shocks driven by CME1+CME2 and CME3. The orange and blue shaded regions indicate the ejecta associated with CME1+CME2 and CME3.

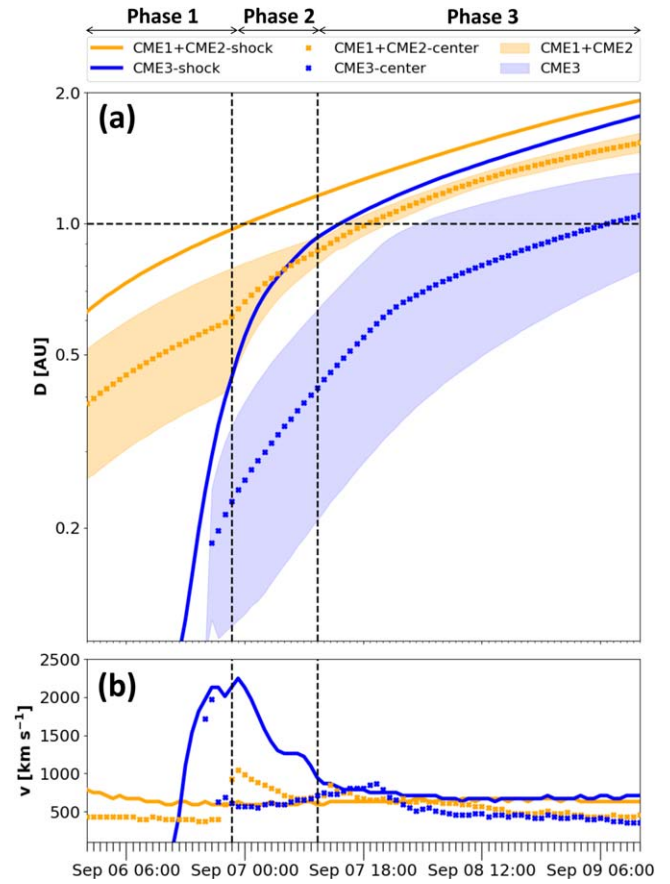


**Figure 8.** Propagation of the shocks and ejecta along the Sun–Earth line in EUHFORIA run 01-01-01. (a): time–distance plot of the shocks and ejecta associated with CME1+CME2 (in orange) and CME3 (in blue) between 0.1 and 2.0 au in EUHFORIA. The solid lines indicate the location of the shocks. The shaded regions indicate the extension of the ejecta. The crosses mark the geometrical center of the ejecta. The horizontal dashed lines mark the 1 au distance. The vertical dashed lines mark the boundaries of the various interaction phases. (b): time–speed plot for the shocks and ejecta centers.

CME1+CME2 (postponing its arrival time) and (2) uncertainties in the CME initial speeds based on the GCS and  $\varphi_r$  reconstructions, which may have contributed to predicting an early arrival time of the shock of CME3 compared with in situ observations (bottom panel in Figure 5). During this phase the shock driven by CME3 enters again a high- $\beta$  ( $\beta > 50$ ) environment, characterized by a low Alfvén speed ( $\sim 15 \text{ km s}^{-1}$ ) and a sound speed comparable to that in the ejecta ( $\sim 95 \text{ km s}^{-1}$ ). The density in the sheath is about 2 orders of magnitude higher than in the ejecta. As the shock enters this new region, its speed with respect to the upstream plasma drops below  $850 \text{ km s}^{-1}$ , due to the increased upstream density. Its radial speed is still slightly larger than the speed of the leading shock driven by CME1+CME2 ( $\sim 800 \text{ km s}^{-1}$  compared with  $\sim 630 \text{ km s}^{-1}$ ), so the CME3-driven shock continues to get closer to the shock ahead, but at a slower rate. We expect them eventually to merge, but the rate of approach is so low that this would take place only beyond the outer boundary of the simulation domain (i.e., beyond 2 au).

Analyzing the energy of each substructure in this phase, we observe that the CME3 shock starts heating and compressing the CME1+CME2 sheath ahead, as indicated by the decrease in its radial size and by the increase in the associated  $\tilde{\epsilon}_{\text{kin}}$ ,  $\tilde{\epsilon}_{\text{mag}}$ , and  $\tilde{\epsilon}_{\text{therm}}$

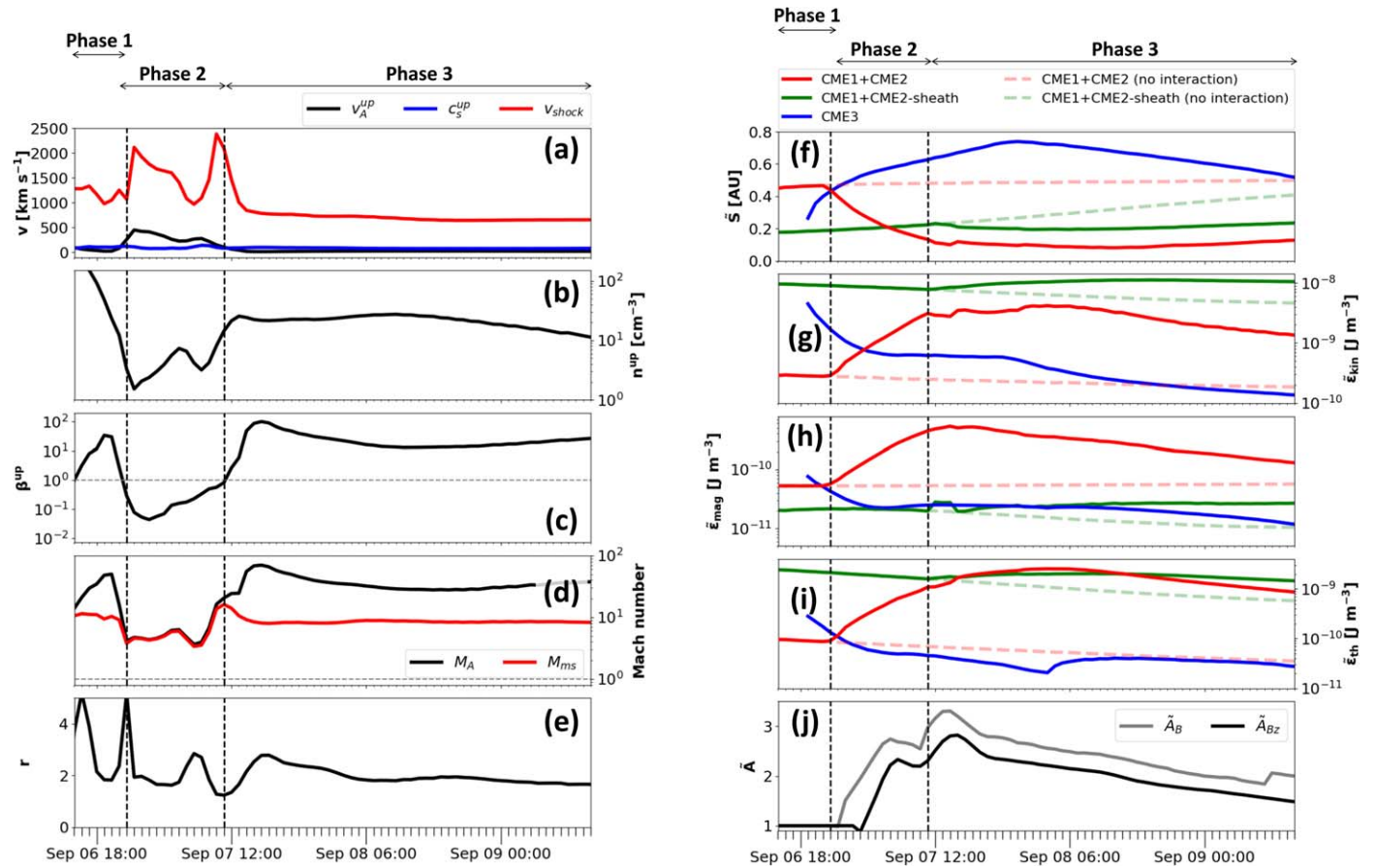


**Figure 9.** Left: panels (a)–(e) show the conditions as observed just upstream of the shock driven by CME3 during its propagation in interplanetary space. Right: panels (f)–(i) show the scaled radial size and the kinetic, magnetic, and thermal energy densities of CME1+CME2 (red), its sheath (green), and CME3 (blue). Panel (j) shows the geoeffectiveness amplification factors ( $\tilde{A}$ ) of CME1+CME2 in terms of  $\tilde{B}$  ( $\tilde{A}_B$ ) and  $\tilde{B}_z$  ( $\tilde{A}_{Bz}$ ) due to the interaction with the shock driven by CME3. The vertical dashed lines mark the boundaries of the various interaction phases.

compared with the simulation without interaction (green continuous and dashed lines in Figures 9(f)–(i)). At the same time, the scaled radial size of CME1+CME2 (CME3) slowly decreases (increases) until September 7 at 23:00 UT, when the trends invert. Most notably, in this phase we also observe that the  $\tilde{A}_B$  and  $\tilde{A}_{Bz}$  amplification factors follow a decreasing trend starting from September 7 at 14:00 UT. We explain this by noting that while  $\tilde{\epsilon}_{mag}$  in CME1+CME2 starts decreasing from September 7 at 14:00 UT, its  $\tilde{\epsilon}_{kin}$  and  $\tilde{\epsilon}_{therm}$  continue increasing until September 8 at 03:00 UT. The earlier peak of  $\tilde{\epsilon}_{mag}$  compared with those of  $\tilde{\epsilon}_{kin}$  and  $\tilde{\epsilon}_{therm}$  suggests a conversion of the magnetic energy accumulated by CME1+CME2 during the shock–ejecta interaction phase, into kinetic and thermal energy of the same structure. The acceleration of CME1+CME2 due to this energy conversion is particularly visible in Figure 9(b). During this energy-conversion phase, the radial size of CME1+CME2 slightly increases as indicated by the constant scaled radial size (Figure 9(g)), most probably due to the presence of CME3 at the back of CME1+CME2 preventing a further expansion. At the end of this phase CME1+CME2 and CME3 move at almost the same speed ( $\sim 670$  km s<sup>-1</sup>, Figure 9(b)). The low expansion of CME1+CME2 is therefore consistent with numerical and observational studies (Xiong et al. 2006, 2007; Gulisano et al. 2010; Lugaz et al. 2012), which highlighted how the expanding behavior of the leading ejecta after the end of the main interaction phase depends on the delicate interplay between the natural tendency for the CME to expand and the compressing action of the trailing ejecta.

The most relevant consequence of the expansion and conversion of magnetic energy into acceleration and heating is that CME1+CME2 progressively “forgets” the amplification of  $B_z$  caused by the interaction with CME3, and it slowly returns to  $B_z$  conditions similar to the case without interaction (“decay phase”). This suggests that one of the key factors at the origin of the intense geomagnetic storm triggered by the 2017 September 4–6 CMEs was their arrival at Earth during the phase of maximum helioeffectiveness amplification due to the interaction of CME1+CME2 with CME3.

#### 4.3. Effect of the Interactions at 1 au

##### 4.3.1. $B_z$ and Arrival Time Predictions

Together with the intensity and orientation of their internal magnetic field at Earth (Savani et al. 2015, 2017; Palmerio et al. 2018), another key CME parameter that the community has long tried to predict is the arrival time (Möstl et al. 2014; Riley et al. 2018; Verbeke et al. 2019a). Current estimates of prediction uncertainties for this parameter are about  $\pm 10$  hr depending on the exact metric considered and on the model used (Riley et al. 2018; Wold et al. 2018), with numbers increasing for more complex events. In the context of interacting CMEs, the arrival time of individual CMEs can be significantly affected by two different effects impacting the CME kinematics: (1) the preconditioning of the ambient solar wind due to the passage of previous CMEs (Temmer et al. 2017) and (2) direct

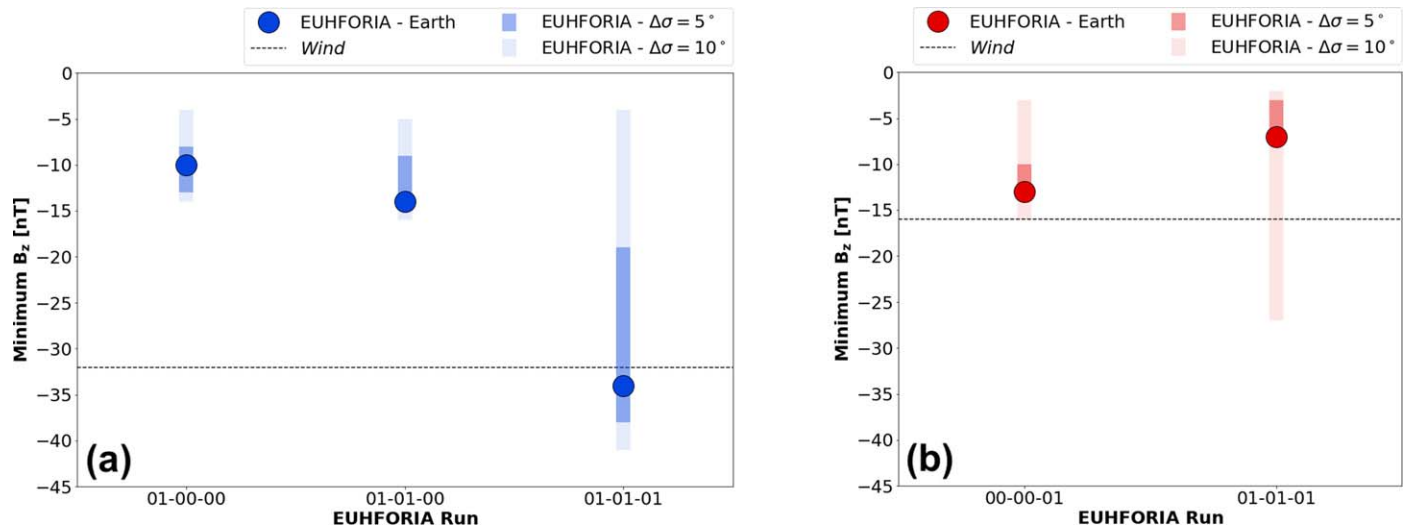


**Figure 10.** Scatter plots summarizing the minimum  $B_z$  predicted from the various EUHFORIA runs for CME1+CME2 (a) and CME3 (b), compared with *Wind* in situ measurements of the minimum  $B_z$  associated with E1 (a) and E2 (b) (black dashed lines). Predictions at Earth are indicated with colored dots, while predictions at virtual spacecraft separated by  $\Delta\sigma = 5^\circ$  and  $\Delta\sigma = 10^\circ$  from Earth are indicated as colored bars.

CME–CME interactions (*CME–CME collisions*; see, e.g., Liu et al. 2014a; Shen et al. 2017). Given the relevance of CME–CME interactions in affecting the kinematics of individual CMEs and, consequently, the prediction of their arrival times at Earth, we address here how much the  $B_z$  and arrival times at Earth of the shocks and ejecta associated with CME1+CME2 and CME3 were affected by their interaction. To do so, we start from the identification of the shocks and ejecta boundaries performed in Section 4.2, and then we extract and compare times at which the shock and leading edge of the ejecta associated with CME3 arrived at 1 au, in simulations with (run 01-01-01) and without (run 00-00-01) the presence of the preceding CMEs. To assess the impact of the interaction on the arrival time of CME1+CME2, we similarly extract and compare the position in time of the shock and leading edge of the ejecta associated with CME1+CME2 obtained from run 01-01-01 and run 01-01-00.

*Effect on CME1+CME2*—In Figure 10(a) we plot the predicted minimum  $B_z$  associated with CME1+CME2 from the EUHFORIA time series at Earth and the surrounding virtual spacecraft, together with the observed minimum  $B_z$  associated with E1 (see Figure 2). We observe that the simulation of CME1 alone (run 01-00-00) predicts a modest minimum  $B_z$  of  $-10$  nT ( $-13$  to  $-8$  nT considering spacecraft separated by an angular distance  $\Delta\sigma = 5^\circ$  from Earth and  $-14$  to  $-4$  nT considering spacecraft separated by  $\Delta\sigma = 10^\circ$ ). While the strength of the magnetic field within CME1 at Earth is similar to the unshocked region in E1, due to its relatively low initial speed compared with CME2 (Table 1), the shock driven by CME1 without the inclusion of CME2 in our simulations is predicted to arrive at Earth on September 7 at 09:33 UT, that is, about 10 hr later than the observed S1. When adding CME2 to the simulations (run 01-01-00), the early interaction of CME1 and CME2 results in a merged structure that propagates in the heliosphere with a speed close to that of the fastest CME involved, that is, CME2, arriving at Earth on September 7 at 02:23 UT, that is, only 3 hr later than the actual arrival time of S1. The predicted minimum  $B_z$  of this combined structure is  $-14$  nT ( $-15$  to  $-9$  nT considering spacecraft separated by  $\Delta\sigma = 5^\circ$  from Earth and  $-16$  to  $-5$  nT considering spacecraft separated by  $\Delta\sigma = 10^\circ$ ), less than 5 nT lower than the unshocked (upstream) region observed in E1. The start of the

ejecta associated with CME1+CME2 is predicted on September 7 at 23:13 UT, only 3 hr later than the starting time of ejecta E1 based on *Wind* in situ observations. When including all three CMEs (run 01-01-01), the predicted minimum  $B_z$  of CME1+CME2 at Earth drops to  $-35$  nT, that is, very close to the minimum observed value of  $-32$  nT. When accounting for uncertainties related to the initial CME directions of propagation, the predicted value varies between  $-38$  and  $-19$  nT for a  $\Delta\sigma = 5^\circ$  separation from Earth and between  $-41$  and  $-4$  nT for a  $\Delta\sigma = 10^\circ$  separation from Earth. Overall, we also observe a good level of agreement between the predicted and the observed  $B$  and  $B_z$  time series at and around Earth (see Appendix C). While the predicted arrival time of the shock driven by CME1+CME2 is unaffected by the inclusion of CME3 in our simulations, the ejecta associated with CME1+CME2 arrives about 5 hr earlier, that is, on September 7 at 17:43 UT. The ejecta is therefore predicted to arrive about 2 hr earlier than the starting time of ejecta E1 based on *Wind* in situ observations. Overall, the very close match between the modeled and observed arrival times and minimum  $B_z$  in run 01-01-01 provides strong evidence that S1 and E1 were indeed the interplanetary counterparts of CME1+CME2.

By comparing the minimum  $B_z$  prediction from runs 01-01-00 and 01-01-01 at and around Earth, we conclude that the presence of S2 and E2 contributed to an increase in the minimum  $B_z$  associated with E1 by a factor of 2.5 (ranging between 2.1 and 2.5 for a  $\Delta\sigma = 5^\circ$  separation from Earth and between 0.8 and 2.6 for a  $\Delta\sigma = 10^\circ$  separation from Earth), a value consistent with the results obtained by Shen et al. (2018) based on observational arguments and with the analysis in Section 4.2.

*Effect on CME3*—For completeness, in Figure 10(b) we plot the predicted minimum  $B_z$  at and around Earth associated with CME3 in a similar way as was already done for CME1+CME2. Simulation results at Earth from run 00-00-01 are consistent with the observed minimum  $B_z$  within E2 ( $-13$  nT compared with  $-16$  nT), while inclusion of the preceding CMEs predicts a minimum  $B_z$  of  $-6$  nT. By considering virtual spacecraft in the vicinity of Earth, however, we observe that predictions vary between  $-6$  and  $-3$  nT for  $\Delta\sigma = 5^\circ$  and between  $-27$  and  $-2$  nT for  $\Delta\sigma = 10^\circ$ . Therefore, although run 00-00-01 gives a slightly better prediction for the minimum  $B_z$  within E2 at Earth,

results in the vicinity of Earth from both simulations are overall consistent with the value measured in situ. The larger spread in the minimum  $B_z$  in the vicinity of Earth predicted in run 01-01-01 compared with run 00-00-01 may reflect the development of finer structures within CME3, or potential deflections in its trajectory, as a consequence of its interaction with CME1+CME2 (or a combination of the two).

Considering its arrival time at Earth, run 00-00-01 predicts the shock of CME3 to arrive at Earth on September 8 at 08:23 UT, followed by the ejecta starting on September 9 at 01:43 UT. As expected, the inclusion of CME1+CME2 ahead of CME3 (run 01-01-01) anticipated the arrival of the shock by about 15 hr to September 7 at 17:03 UT, and the arrival of the ejecta by about 16 hr, to September 8 at 09:43 UT. This was caused by the solar wind preconditioning induced by CME1+CME2 (which also contributed to the early start of the interaction). These final predictions match well the observed arrival time of S2 (September 7 at 22:38 UT, about 6 hr later than predicted) and the starting time of E2 (September 8 at 11:00 UT, about 1 hr later than predicted) at *Wind*, supporting their association with CME3 at the Sun. At the same time, we note how the predicted long duration of the ejecta associated with CME3 in run 01-01-01 suggests that it was associated with both the E2 and E3 (see Figure 2), supporting the interpretation that they were indeed both associated with the same CME at the Sun.

#### 4.3.2. Dst Predictions and Geoeffectiveness

To quantify the effect of CME–CME interactions on the actual impact of the merged CME1+CME2 structure on Earth (i.e., its geoeffectiveness), we apply the method presented in Section 3.4 to the EUHFORIA time series extracted at and around the location of Earth. To better quantify by how much EUHFORIA-based Dst predictions are off due to mispredictions of the CME impact parameters, and how much of the discrepancy is actually due to limitations of the specific coupling function used, we also apply the coupling function to *Wind* in situ measurements. As previously done for the minimum  $B_z$ , we separately discuss the predictions obtained for CME1+CME2 (Figure 11(a)) and for CME3 (Figure 11(b)).

*Minimum Dst Associated with CME1+CME2*—As already found for the  $B_z$  prediction, Dst predictions associated with CME1+CME2 are highly dependent on the simulated CMEs in different runs (Figure 11(a)). While CME1 alone (run 01-00-00) predicts a minimum Dst of  $-99$  nT ( $-125$  to  $-69$  nT considering spacecraft separated by  $\Delta\sigma = 5^\circ$  from Earth and  $-135$  to  $-16$  nT considering spacecraft separated by  $\Delta\sigma = 10^\circ$ ), the addition of CME2 (run 01-01-00) leads to a predicted minimum Dst of  $-119$  nT ( $-128$  to  $>0$  nT considering spacecraft separated by  $\Delta\sigma = 5^\circ$  from Earth and  $-134$  to  $>0$  nT considering spacecraft separated by  $\Delta\sigma = 10^\circ$ ) due to the early interaction between CME1 and CME2. The simulation including all three CMEs (run 01-01-01) finally provides us with an estimate of the contribution of CME–CME interaction processes between CME1+CME2 and CME3 to the geoeffectiveness of CME1+CME2. In particular, we note that the minimum Dst predicted at Earth is  $\sim -215$  nT. When accounting for uncertainties related to the initial CME directions of propagation, the predicted value varies between  $-227$  and  $-123$  nT for a  $\Delta\sigma = 5^\circ$  separation from Earth and between  $-229$  and  $-33$  nT for a  $\Delta\sigma = 10^\circ$  separation from Earth. By comparing the minimum Dst prediction from runs 01-01-00 and 01-01-01 at and around Earth, we conclude that the presence of S2 and E2 significantly enhanced the

geoeffectiveness of E1 by enhancing the minimum Dst by a factor of 1.8 (ranging between 1.7 and 1.8 for a  $\Delta\sigma = 5^\circ$  separation from Earth and between 1.7 and 1.3 for a  $\Delta\sigma = 10^\circ$  separation from Earth, consistent with Shen et al. 2018). In terms of absolute values, the minimum Dst recorded on ground was  $-142$  nT, while the predicted minimum based on *Wind* in situ measurements was  $-149$  nT, that is, the two values are very close. Therefore, we observe that EUHFORIA run 01-01-01 tends to overestimate the Dst at Earth by a factor of 1.5 compared with actual observations (1.4 when compared with *Wind* predictions). The overprediction is significantly higher than the one observed in  $B_z$  (1.1 compared with *Wind* observations), most probably due to the larger density (entering the calculation of Dst via the solar wind dynamic pressure ( $P_{\text{dyn}}$ ); see Equation (3) in O’Brien & McPherron 2000b) predicted by EUHFORIA (see Appendix C).

*Minimum Dst Associated with CME3*—For completeness, in Figure 11(b) we plot the predicted minimum Dst at and around Earth associated with CME3 in a similar way as was already done for CME1+CME2. Dst estimates reflect what is already found for  $B_z$ , that is, that the magnetic field strength within CME3 was not significantly altered by the interaction process, as the minimum Dst predicted in runs with (run 00-00-01) and without (run 01-01-01) the preceding CME1+CME2 are consistent with each other and with actual observations and *Wind*-based predictions. We also observe an anticorrelation between the minimum  $B_z$  and the minimum Dst predicted in runs 00-00-01 and 01-01-01: while the minimum  $B_z$  increases in the immediate surroundings of Earth, the minimum Dst decreases. This result is most probably due to the combination of the higher density and speed associated with CME3 in run 01-01-01 compared with run 00-00-01 (contributions due to dynamic pressure ( $P_{\text{dyn}}$ ) and the dawn-to-dusk component of the electric field ( $VB_s$ ); see Equations (2) and (3) in O’Brien & McPherron 2000b) and the fact that in run 01-01-01 the Dst dip caused by CME3 started from a condition of highly disturbed Dst already (see also Kamide et al. 1998; Vennerstrom et al. 2016).

#### 4.4. Implications for Space Weather Events at Other Locations in the Heliosphere

From Section 4.2 we concluded that one of the key factors at the origin of the intense storm triggered by the 2017 September 4–6 CMEs was their arrival at Earth during the phase of maximum amplification of the southward  $B_z$  (and consequently, of their helio/geoeffectiveness) due to the interaction of CME1+CME2 with CME3. Moreover, Figure 9(j) highlights the existence of a correlation between the evolutionary phase of CME–CME interactions and the amplification of the helioeffectiveness of the leading ejecta involved in the interaction, at least for the specific CME events and the specific (Sun-to-Earth) direction under study.

In general, for two generic CMEs launched in approximately the same direction, the spatial/temporal windows of the various interaction phases depend on three main parameters: (1) the ambient solar wind through which the CMEs (particularly the preceding one) are propagating, (2) the time interval between the eruptions of the individual CMEs involved, and (3) their relative speed. Therefore, we note that different combinations of such parameters will lead the ejecta to reach Earth or any other location in the heliosphere at different evolutionary phases and hence during different phases of helioeffectiveness amplification. An extensive exploration of the parameter space was performed by Xiong et al. (2007) via 2.5D simulations of interacting CMEs varying the time interval between the eruptions (from 10 to 44 hr) and their relative speeds (from 50 to  $800 \text{ km s}^{-1}$ ). By

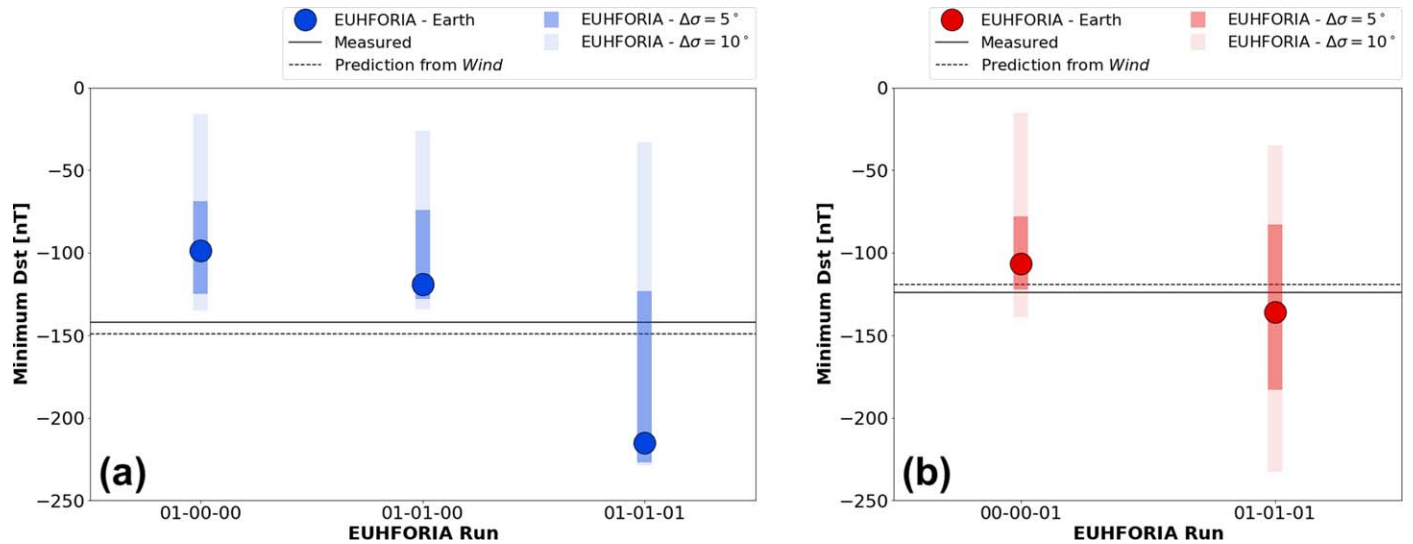


**Figure 11.** Scatter plots summarizing the minimum Dst predicted from the EUHFORIA runs at Earth for CME1+CME2 (a) and CME3 (b), compared with predictions from *Wind* in situ measurements associated with E1 and E2 (black dashed lines), and the minimum Dst measured at Earth (black solid lines). EUHFORIA predictions at Earth are indicated with colored dots, while predictions at virtual spacecraft separated by  $\Delta\sigma = 5^\circ$  and  $\Delta\sigma = 10^\circ$  from Earth are indicated as colored bars.

comparing the resulting geoeffectiveness amplification at Earth in the case of interactions that reached 1 au at different evolutionary stages, they similarly suggested that the evolution stage may be a dominant factor in determining the ultimate geoeffectiveness of interacting CMEs, although a comparison of model results with in situ observations of real CME events was not presented. They also suggested that the exact evolution profile in spacetime of the helioeffectiveness amplification may depend on the impact angle between the spacecraft crossing and the CME apex, with spacecraft locations close to the CME nose more likely to maintain the helioeffectiveness amplification due to the persistent push of the trailing ejecta on the leading ejecta (preventing further expansion of the latter) and spacecraft locations close to the CME flanks exhibiting a decay of the helioeffectiveness amplification due to the narrower extension of the trailing magnetic ejecta compared with its driven shock (which induced the compression). An in-depth analysis of such angular dependencies in EUHFORIA simulations is left for future studies.

The existence of a decay phase in the helioeffectiveness amplification starting after the end of the shock–ejecta interaction clearly has strong implications for the impact of CME–CME interactions at various locations in the heliosphere. In particular, each CME–CME interaction event may be associated with a “helioeffectiveness amplification zone,” corresponding to the heliocentric distances associated with the maximum amplification phase for a given combination of CME waiting times and relative speeds. The amplification of the helioeffectiveness of individual CMEs will be null for spacecraft locations closer to the Sun than the distance at which the interaction starts, it will progressively increase for spacecraft locations between the start and the end of the shock–ejecta interaction (growth phase), it will be maximal for spacecraft locations at the outer edge of this distance range (maximum phase), and it will progressively decrease for spacecraft locations farther away from the Sun (decay phase). Although a more extensive study of this impact needs to be addressed in a future work, we speculate that the nonuniform probability distribution of the CME waiting times and relative speeds (Wang et al. 2013) may also result in higher probabilities of having helioeffective CME–CME interaction events at specific heliocentric distances than at others.

## 5. Summary and Conclusions

In this work we have performed a comprehensive Sun-to-Earth analysis of three successive CMEs that erupted from AR 12673 during a remarkably active week in early 2017 September and that resulted in an intense two-step geomagnetic storm (main dip:  $Dst_{\min} = -142$  nT; secondary dip:  $Dst_{\min} = -124$  nT) driven by the interplanetary interactions occurring among the CMEs involved. Together with the analysis of the CME-related signatures at the source region, in the corona, and at L1, we have also performed global simulations in the heliosphere using the spheromak CME model in EUHFORIA initialized with observation-based kinematic, geometric, and magnetic parameters for the CMEs.

Remote-sensing observations show that the first two CMEs (CME1 and CME2) were sympathetic events that erupted less than 3 hr apart, with CME2 being faster than CME1 by  $\sim 500$  km  $s^{-1}$ . They interacted already in the upper corona (around  $20 R_{\odot}$ ), and they subsequently propagated through the heliosphere as a merged structure. CME3 erupted about 2 days later with a speed in the corona of  $\sim 2000$  km  $s^{-1}$ , that is,  $\sim 500$  km  $s^{-1}$  faster than CME2, eventually catching up with the two preceding CMEs in the heliosphere.

Modeling results allowed us to associate the interplanetary shock driven by CME1+CME2 with the shock observed at L1 on September 6 at 23:13 UT (S1) and the CME1+CME2 structure with the magnetic ejecta observed starting on September 7 at 20:00 UT (E1). The interplanetary shock on September 7 at 22:38 UT (S2) was most likely driven by the following CME3, and it was propagating through the preceding CME1+CME2 ejecta. Simulation results also supported the interpretation that both the E2 and E3 observed in situ at L1 were associated with CME3 at the Sun.

By comparing EUV observations of the source region and in situ observations at L1, we also found that the chirality of the flux ropes in the source AR was consistent with the chirality of the flux rope inferred from in situ observations at Earth, providing additional support to our linking of structures at the Sun with their interplanetary counterparts. On the other hand, we found significant rotations between the flux rope orientations at the source region, in the corona, and at 1 au, which are most probably due to the interaction processes occurring

among the three CMEs involved at various stages during their propagation. Because of the difficulties in constraining the flux rope orientations at 0.1 au, that is, at the distance of the inner boundary of our heliospheric simulation domain, we tested CME simulations using different orientations, ultimately finding that the initialization of CMEs as ESW flux rope types at 0.1 au generated the best predictions at Earth.

To initialize the toroidal magnetic flux  $\varphi_t$  of the spheromak CMEs in our simulations, we tested a combination of observational methods to determine the reconnected flux  $\varphi_r$  associated with each eruption in a more robust way. The results from the application of statistical relations between the main flare and CME properties (such as the flare peak intensity and the CME 3D speed) and different posteruptive signatures were found to be, on average, compatible with the results from more sophisticated single-event analyses. This result is particularly relevant for space weather forecasting purposes, as it suggests a quick and easy to apply method to initialize the magnetic field strength in flux rope CME models that can be potentially applied routinely by forecasters or even via automatic algorithms.

An analysis of the interaction of CME1+CME2 and CME3 based on 3D simulation results shows that the interaction between the shock driven by CME3 and the preceding magnetic ejecta formed by the merging of CME1 and CME2 started around 0.45 au (on September 6 at 22:00 UT). Analyzing the impact of the shock–ejecta interaction on the amplification of the  $B_z$  magnetic field (i.e., *helioeffectiveness*) of CME1+CME2 at various times/heliocentric distances along the Sun–Earth line, we found it could be characterized by a growth phase, a maximum phase, and a decay phase. For the particular event considered, a maximum helioeffectiveness amplification of 2.8 for the minimum  $B_z$  was reached near 0.9 au, that is, close to Earth’s location. This amplification phase was also found to be associated with the compression, acceleration, and heating of CME1+CME2 by the shock driven by CME3. The growth and maximum phases were followed by a slow decay at larger heliocentric distances, which was associated with the conversion of magnetic energy into kinetic and thermal energy of CME1+CME2. The helioeffectiveness amplification had almost completely disappeared by the time the merged CME1+CME2+CME3 structure reached 1.8 au.

The simulation results showed that the impact of CME1+CME2 on Earth (*geoeffectiveness*) was amplified by the interaction with CME3 by a factor of 2.5 for the minimum  $B_z$  and by a factor of 1.8 for the minimum Dst index, consistent with the recent observational study of this event by Shen et al. (2018). Moreover, while impacting Earth, the system was found to be close to the maximum helioeffectiveness amplification reached at the end of the shock–ejecta interaction phase. We therefore concluded that one of the key factors for causing the event to result in the intense storm on 2017 September 7–8 was the arrival of the CMEs at 1 au during this evolutionary phase. Also, CME3 arrived about 15 hr earlier because of the interaction with the preceding ejecta, that is, the interaction significantly impacted the arrival time prediction for the trailing ejecta.

Overall, the simulation of the three CMEs was able to reproduce the main features in the speed, density, and magnetic field observed profiles at Earth/1 au with a good level of agreement. In terms of CME *geoeffectiveness*, the model predicted a minimum  $B_z$  of  $-35$  nT in association with E1, matching the value observed by *Wind* at L1 (i.e.,  $-32$  nT, in association with E1) remarkably well. The predicted minimum Dst index was a factor of 1.5 higher than the minimum

observed value (1.4 when compared with Dst index predictions based on *Wind* solar wind measurements), most probably as a consequence of an overestimated dynamic pressure, but still consistent with observations within the error bars given by the virtual spacecraft located in the surroundings of Earth.

Significantly advancing our previous knowledge of CME–CME interactions and their influence on the *geoeffectiveness* of individual CMEs depending on the interaction phase, this work shows evidence, for the first time, of the spacetime evolution of the *helioeffectiveness* amplification of a real CME event using 3D simulations in a realistic setup. In general, the exact location in spacetime of each of such phases is primarily determined by the time interval between the successive eruptions and by the relative speed of the individual CMEs involved (in addition to the solar wind conditions ahead of the first CME launched), which ultimately constrain the heliocentric distances of the “*helioeffectiveness* amplification zone,” that is, the region of space associated with the maximum *helioeffectiveness* amplification. This is expected to be maximal for spacecraft/planet locations impacted by the CMEs close to the end of the shock–ejecta interaction phase, and its location will vary depending on the CME waiting times and relative speeds of the specific event considered.

Although a more detailed investigation of this impact needs to be addressed in a future study, because of the nonuniform probability distribution of the CME waiting times and relative speeds, we speculate that higher probabilities of having *helioeffective* CME–CME interaction events may be found at given heliocentric distances rather than others, that is, there could be a range of heliocentric distances where the impact of interaction phenomena on the individual CME *helioeffectiveness* can be expected to be higher than others. This may be of great relevance for current and future explorations of new regions of the inner and outer solar system, for example, from the *Parker Solar Probe*, *Solar Orbiter*, and the *Voyager* missions; and for predictions of space weather events at other planets.

C.S. and E.C. acknowledge funding by the Research Foundation—Flanders (FWO) (grant Nos. 1S42817N and 12M0119N). M.T., K.D., and A.M.V. acknowledge funding by the Austrian Space Applications Programme of the Austrian Research Promotion Agency FFG (ASAP-11 4900217 CORDIM, ASAP-13 859729 SWAMI, and ASAP-14 865972 SSCME). E.K.J.K. acknowledges the Academy of Finland project SMASH 310445. E.K.J.K. and J.P. acknowledge the SolMAG project (ERC-COG 724391) funded by the European Research Council (ERC) in the framework of the Horizon 2020 Research and Innovation Programme, the BRAIN-be project CCSOM. The work of E.K.J.K., E.P., and J.P. has been achieved under the framework of the Finnish Centre of Excellence in Research of Sustainable Space (Academy of Finland grant No. 312390). M.D. acknowledges support by the Croatian Science Foundation under the project 7549 (MSOC) and EU H2020 grant agreement No. 824135 (project SOLARNET). J.G. is supported by the Key Research Program of the Chinese Academy of Sciences (grant Nos. XDPB11 and QYZDB-SSW-DQC015). L.R. thanks the European Space Agency (ESA) and the Belgian Federal Science Policy Office (BELSPO) for their support in the framework of the PRODEX Programme. This work was made possible thanks to the Solar-Terrestrial Centre of Excellence, a collaborative framework funded by the Belgian Science Policy Office. S.P. was funded by KU Leuven and via the projects C14/19/089 (Internal Funds KU Leuven), G.0A23.16N (FWO), and C 90347 (ESA PRODEX). EUHFORIA is developed as a joint

effort between the University of Helsinki and KU Leuven. The full validation of the solar wind and CME modeling is being performed within the CCSOM project (<http://www.sidc.be/ccsom/>). The EUHFORIA website, including a repository for simulation results and the possibility for users to access the code, is currently under construction; please contact the authors for full 3D simulation outputs and model details. The simulations were carried out at the VSC, Flemish Supercomputer Center, funded by the Hercules foundation and the Flemish Government, Department EWI.

*Facilities:* SDO (AIA, HMI); SOHO (LASCO); STEREO (SECCHI); Wind (MFI, SWE); DSCOVR (PlasMag).

*Software:* EUHFORIA (Pomoell & Poedts 2018); Python SunPy (SunPy Community et al. 2015); IDL SolarSoft (Freeland & Handy 1998); ESA JHelioviewer (Müller et al. 2017).

### Appendix A Graduated Cylindrical Shell Analysis

In the following we describe the method used to recover the radial and expansion speed from the GCS fitting of the CMEs under study (shown in Figure 12), first described by Scolini et al. (2019). Using the same notation as Thernisien (2011), the heliocentric distance of the CME front at its apex,  $h_{front}$ , is

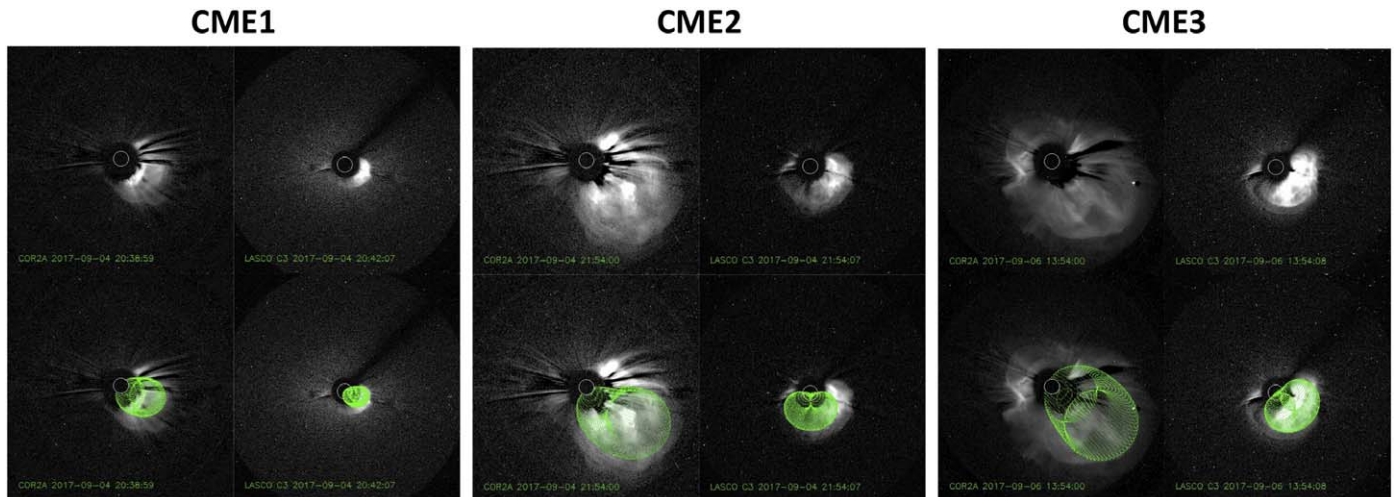


**Figure 12.** LASCO/C3 and STEREO/COR2-A pre-event background-subtracted intensity images of CME1 (left; on 2017 September 4 around 20:39 UT), CME2 (middle; on 2017 September 4 at 21:54 UT), and CME3 (right; on 2017 September 6 at 13:54 UT), with and without the GCS model wire frame (in green).

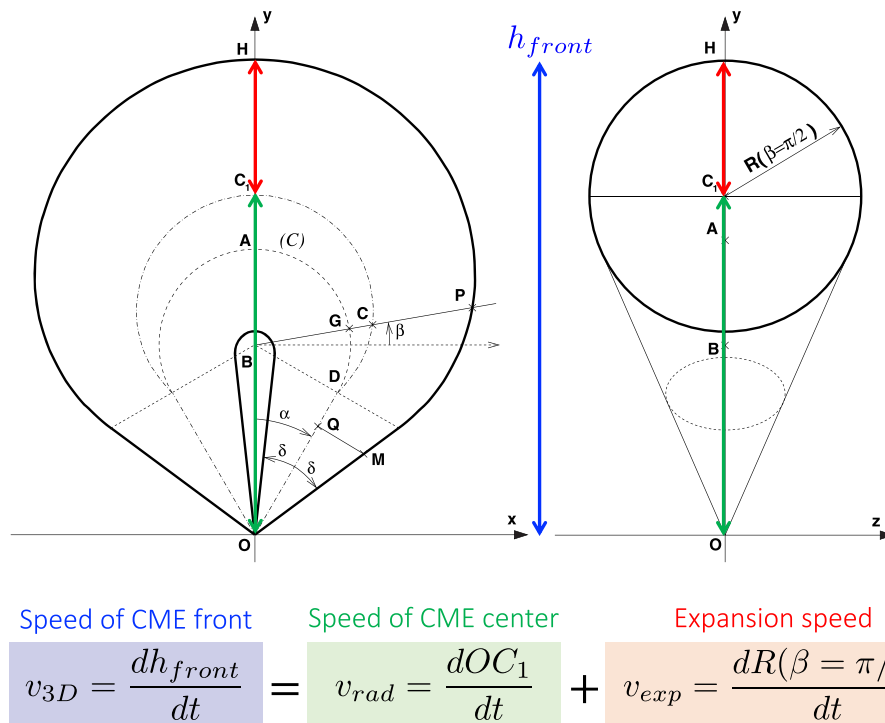


**Figure 13.** Schematic of the GCS model, adapted from Scolini et al. (2019) and Thernisien (2011): face-on (left) and edge-on (right) representations. In the case  $\alpha = 0$ , the face-on and edge-on views coincide. The blue double arrow marks the height of the CME front, the green double arrow marks the height of the CME center, and the red double arrow marks the CME radius. Their variation in time can be used to estimate the total ( $v_{3D} = v_{rad} + v_{exp}$ ), radial ( $v_{rad}$ ), and expansion speed ( $v_{exp}$ ), as described by the relations in the colored boxes.

defined as

$$h_{\text{front}} = OH = \frac{b + \rho}{1 - \kappa}, \quad (9)$$

where  $b = OB$  and  $\rho = BD$ . At the same time, from geometrical considerations we observed that

$$OH = OC_1 + R(\beta = \pi/2), \quad (10)$$

and that the total speed of the CME apex  $v_{3D}$  can be related to the variation over time of the parameter  $h_{\text{front}}$ , the expansion speed  $v_{\text{exp}}$  can be related to the variation in time of  $R(\beta = \pi/2)$ , and the radial speed  $v_{\text{rad}}$  can be related to that of  $OC_1$  (Figure 13). Therefore, the radial and expansion speed can be calculated based on the standard GCS output parameters as

$$\begin{cases} v_{\text{rad}} = \frac{dOC_1}{dt} \\ v_{\text{exp}} = \frac{dR(\beta = \pi/2)}{dt} \end{cases} \quad (11)$$

The heliocentric distance of the apex center,  $OC_1$ , and the cross section radius of the apex,  $R(\beta = \pi/2)$ , are in turn related to the leading edge height  $h_{\text{front}}$  by the following relations (Thernisien 2011):

$$\begin{cases} OC_1 = \frac{b + \rho}{1 - \kappa^2} = \frac{1}{1 + \kappa} h_{\text{front}} \\ R(\beta = \pi/2) = \frac{b + \rho}{1 - \kappa^2} \kappa = \frac{\kappa}{1 + \kappa} h_{\text{front}} \end{cases} \quad (12)$$

so that  $OC_1 + R(\beta = \pi/2) = OH$  (as shown in Figure 13). Combining these results and remembering that all the GCS parameters are in principle time dependent, one obtains

$$v_{\text{rad}} = \frac{d}{dt} \left( \frac{h_{\text{front}}}{1 + \kappa} \right) = \frac{1}{1 + \kappa} \frac{dh_{\text{front}}}{dt} - h_{\text{front}} \frac{1}{(1 + \kappa)^2} \frac{d\kappa}{dt}, \quad (13)$$

and

$$\begin{aligned} v_{\text{exp}} &= \frac{d}{dt} \left( \frac{\kappa}{1 + \kappa} h_{\text{front}} \right) \\ &= \frac{\kappa}{1 + \kappa} \frac{dh_{\text{front}}}{dt} + h_{\text{front}} \left( \frac{1}{1 + \kappa} - \frac{\kappa}{(1 + \kappa)^2} \right) \frac{d\kappa}{dt}. \end{aligned} \quad (14)$$

For CMEs where  $\kappa$  can be kept fixed in time, the above equations simplify to

$$v_{\text{rad}} = \frac{1}{1 + \kappa} \frac{dh_{\text{front}}}{dt}, \quad (15)$$

and

$$v_{\text{exp}} = \frac{\kappa}{1 + \kappa} \frac{dh_{\text{front}}}{dt}. \quad (16)$$

## Appendix B

### EUHFORIA Results on the Ecliptic and Meridional Planes

Figures 14–18 show the results of EUHFORIA simulations on the ecliptic plane and on the meridional plane containing Earth, for each of the five runs performed (Table 2).

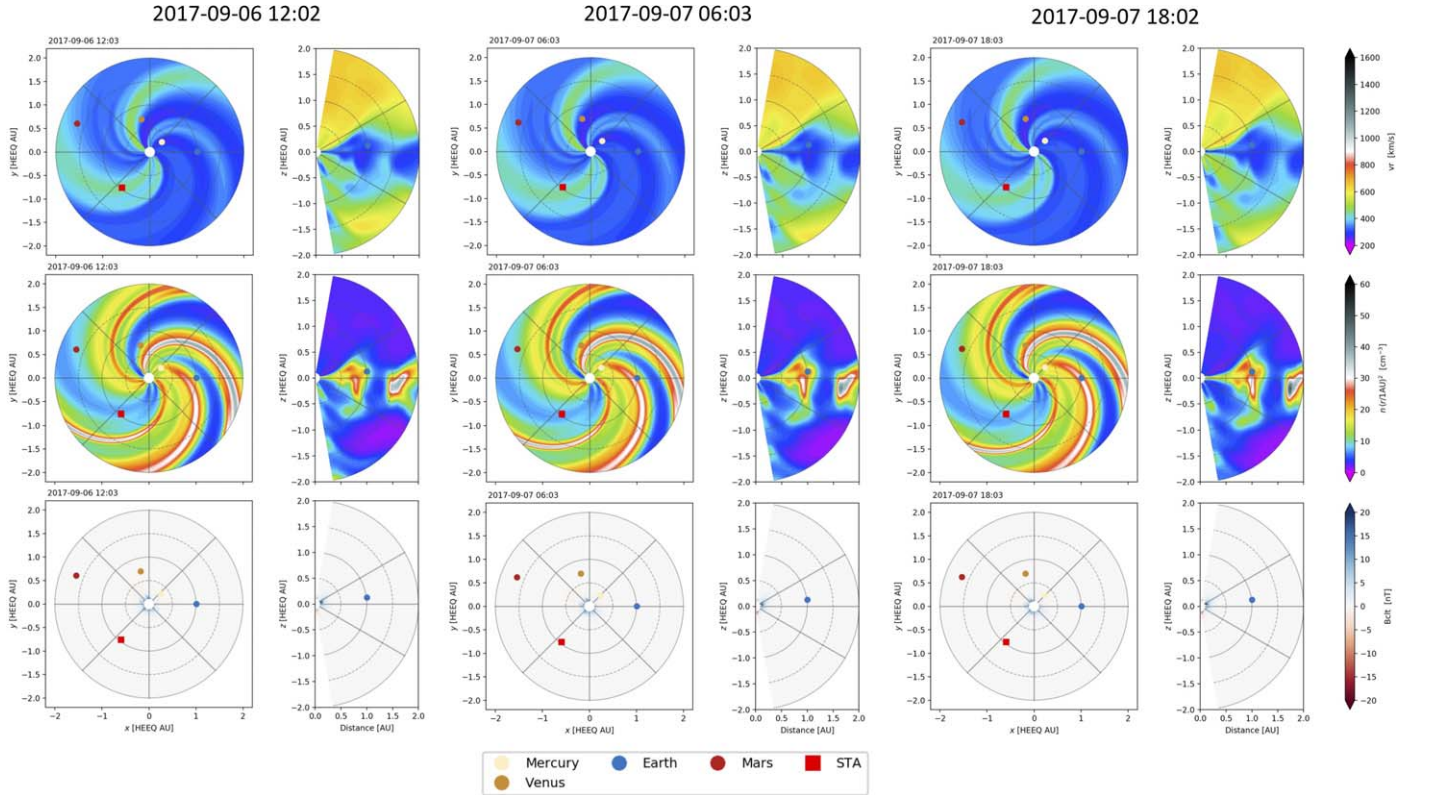


**Figure 14.** Snapshots from EUHFORIA run 00-00-00 showing the radial speed ( $v_r$ , top row), scaled number density ( $n(D/1 \text{ au})^2$ , middle row), and colatitudinal magnetic field ( $B_{\text{clt}}$ , bottom row) in the heliographic equatorial plane and in the meridional plane that includes Earth (which is indicated by solid blue circles). Left column: 2017 September 6 at 12:02 UT. Middle column: 2017 September 7 at 06:03 UT. Right column: 2017 September 7 at 18:02 UT.

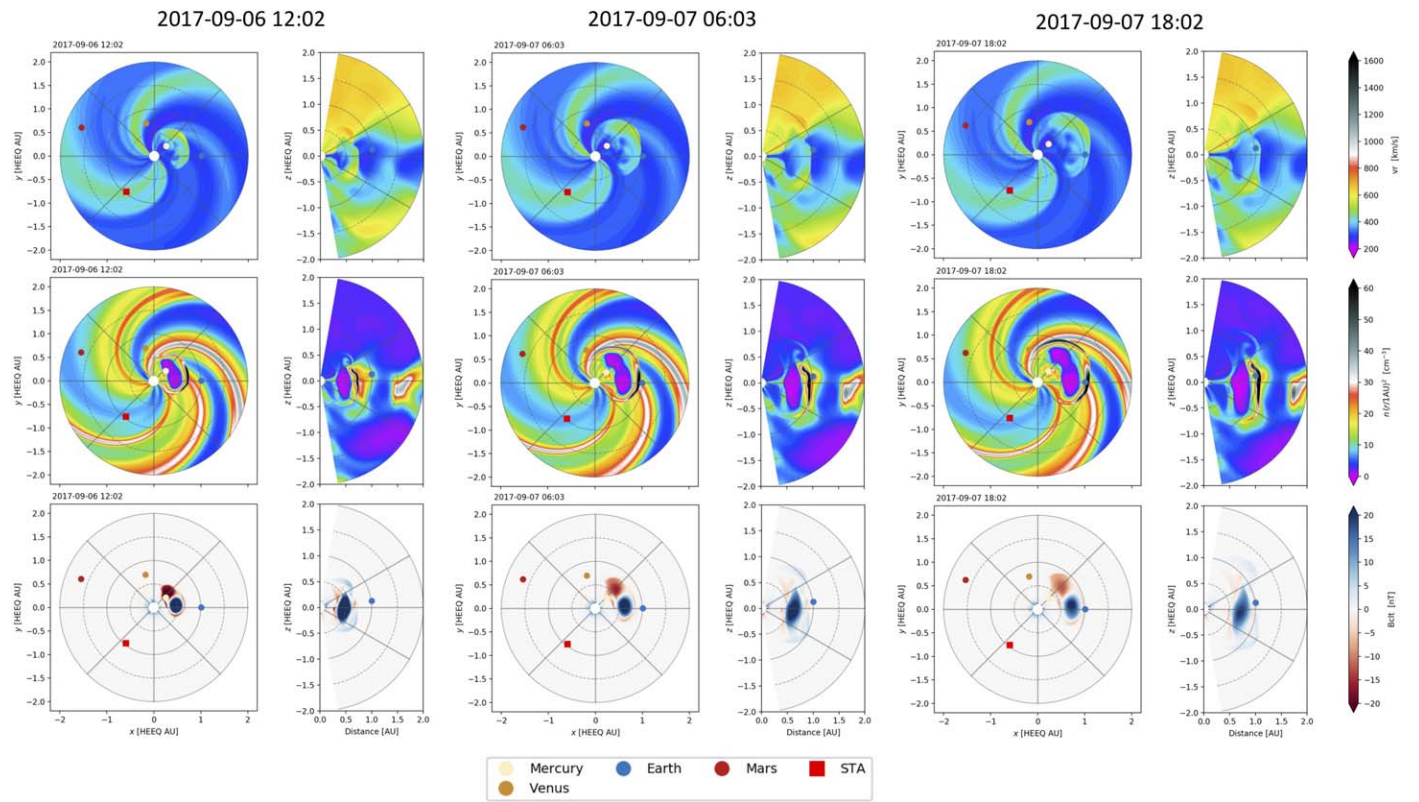


**Figure 15.** Snapshots from EUHFORIA run 01-00-00 showing the radial speed ( $v_r$ , top row), scaled number density ( $n(D/1 \text{ au})^2$ , middle row), and colatitudinal magnetic field ( $B_{\text{clt}}$ , bottom row) in the heliographic equatorial plane and in the meridional plane that includes Earth (which is indicated by solid blue circles). Left column: 2017 September 6 at 12:02 UT. Middle column: 2017 September 7 at 06:03 UT. Right column: 2017 September 7 at 18:02 UT.

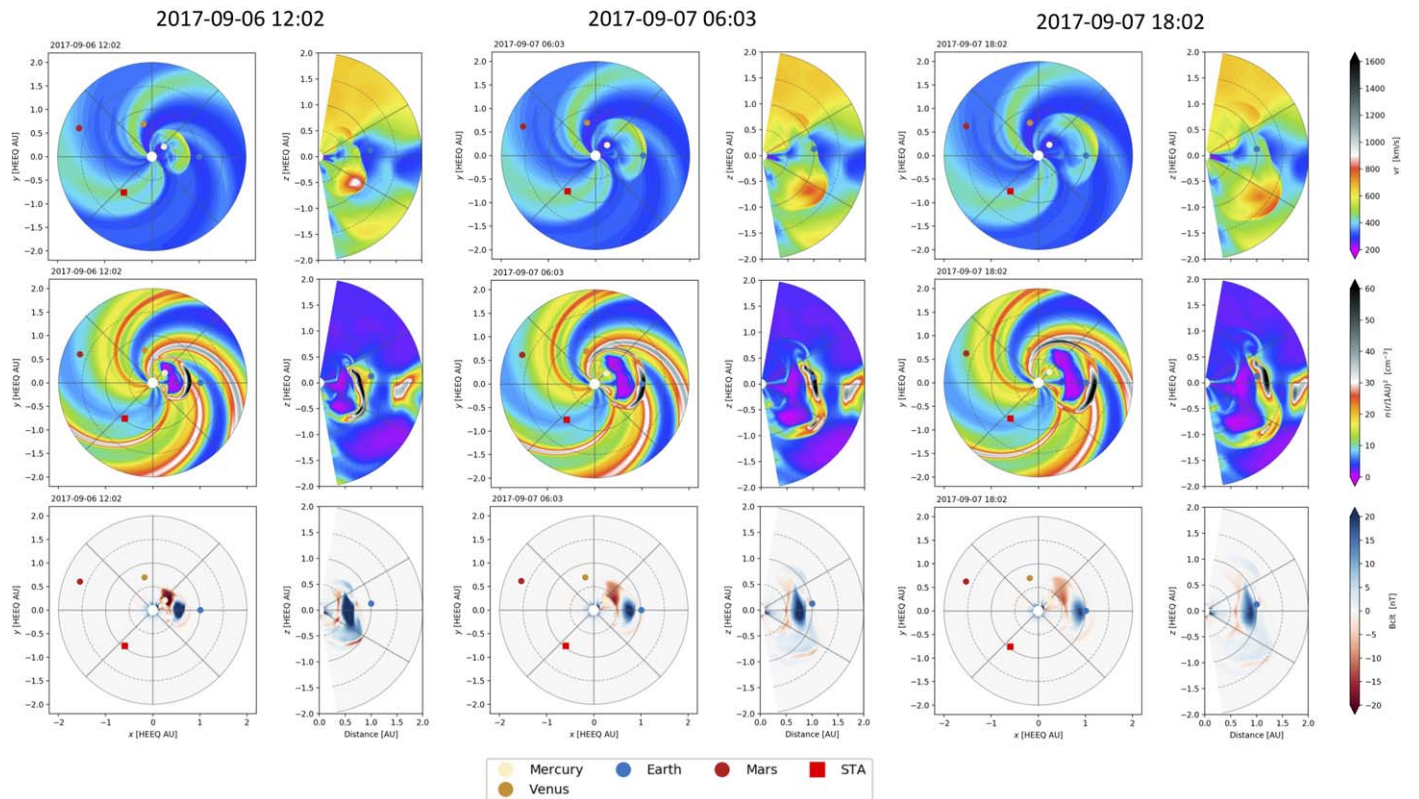


**Figure 16.** Snapshots from EUHFORIA run 01-01-00 showing the radial speed ( $v_r$ , top row), scaled number density ( $n(D/1 \text{ au})^2$ , middle row), and colatitudinal magnetic field ( $B_{\text{clt}}$ , bottom row) in the heliographic equatorial plane and in the meridional plane that includes Earth (which is indicated by solid blue circles). Left column: 2017 September 6 at 12:02 UT. Middle column: 2017 September 7 at 06:03 UT. Right column: 2017 September 7 at 18:02 UT.

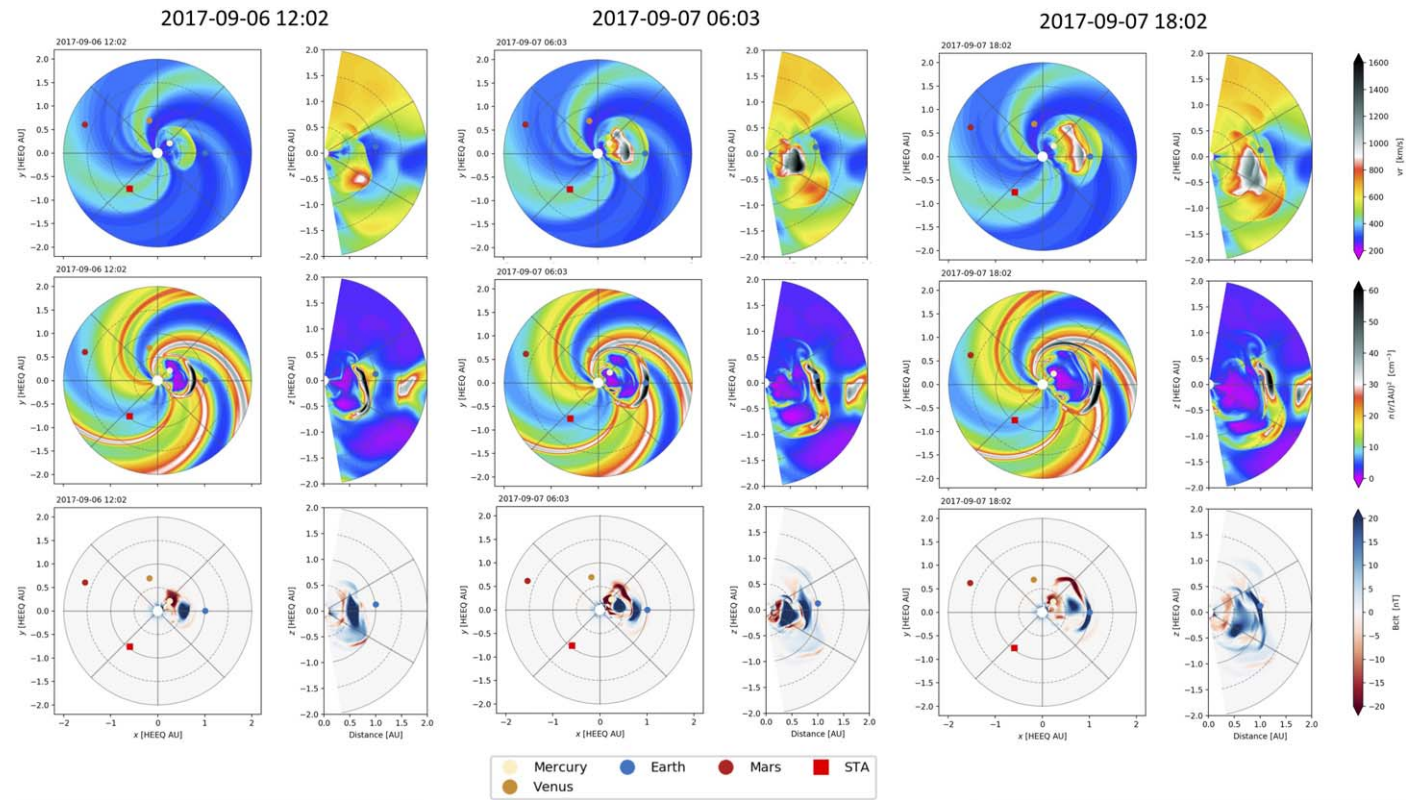


**Figure 17.** Snapshots from EUHFORIA run 01-01-01 showing the radial speed ( $v_r$ , top row), scaled number density  $(n(D/1 \text{ au})^2$ , middle row), and colatitudinal magnetic field ( $B_{\text{col}}$ , bottom row) in the heliographic equatorial plane and in the meridional plane that includes Earth (which is indicated by solid blue circles). Left column: 2017 September 6 at 12:02 UT. Middle column: 2017 September 7 at 06:03 UT. Right column: 2017 September 7 at 18:02 UT.

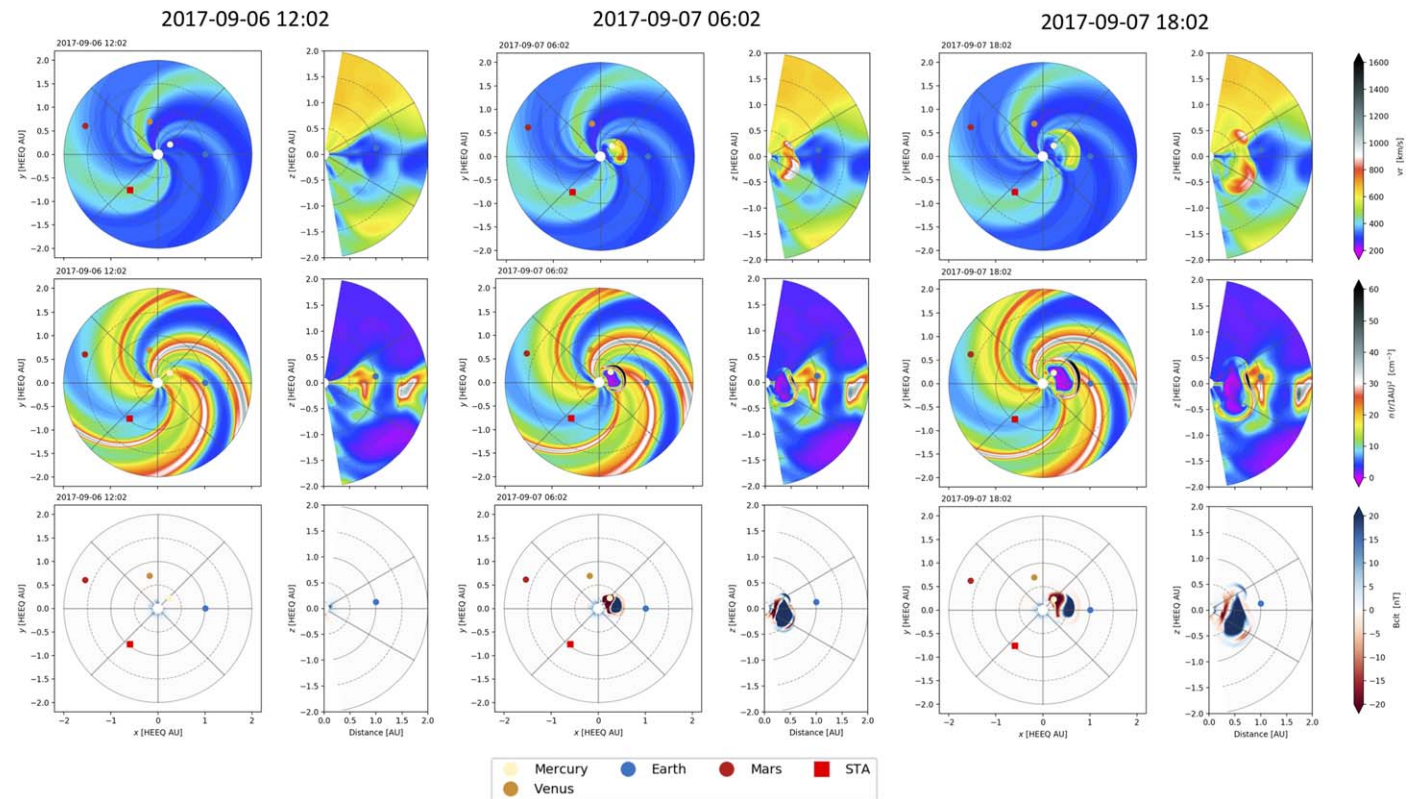


**Figure 18.** Snapshots from EUHFORIA run 00-00-01 showing the radial speed ( $v_r$ , top row), scaled number density  $(n(D/1 \text{ au})^2$ , middle row), and colatitudinal magnetic field ( $B_{\text{col}}$ , bottom row) in the heliographic equatorial plane and in the meridional plane that includes Earth (which is indicated by solid blue circles). Left column: 2017 September 6 at 12:02 UT. Middle column: 2017 September 7 at 06:03 UT. Right column: 2017 September 7 at 18:02 UT.

### Appendix C EUHFORIA Predictions at Earth

Figures 19 and 20 show the time series extracted from EUHFORIA at Earth and surrounding virtual spacecraft,

together with the predicted Dst index, for each of the five runs performed (Table 2). *Wind* in situ measurements at L1 and Dst measurements at Earth are included for comparison.

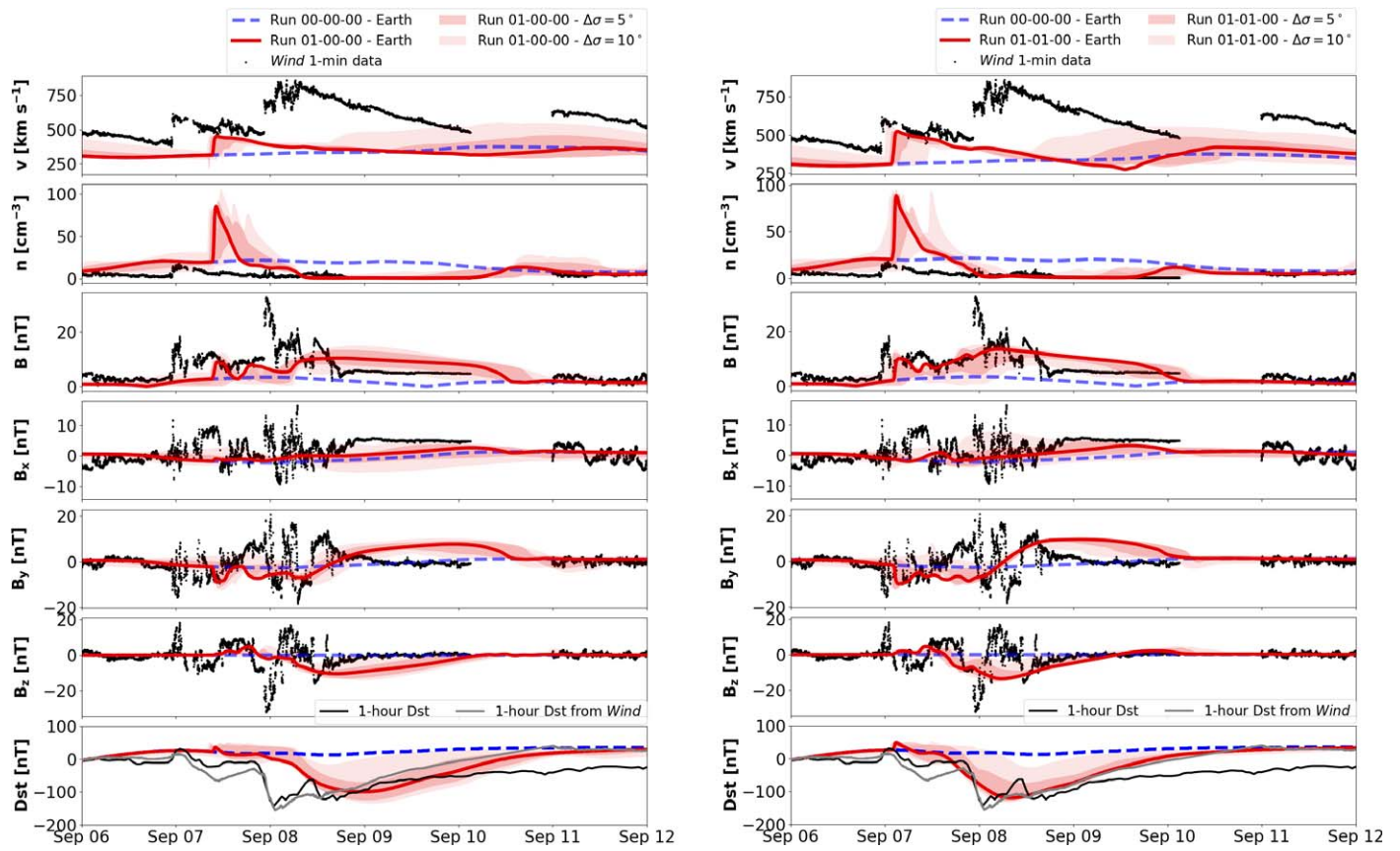


**Figure 19.** Comparison of EUHFORIA time series (red and blue) with in situ measurements from *Wind* (black) for the whole temporal computational domain (both in GSE coordinates). The bottom panel shows a comparison of the measured Dst index (black) with predictions obtained from solar wind measurements at *Wind* (gray) and from EUHFORIA time series after conversion into GSM coordinates (red and blue).

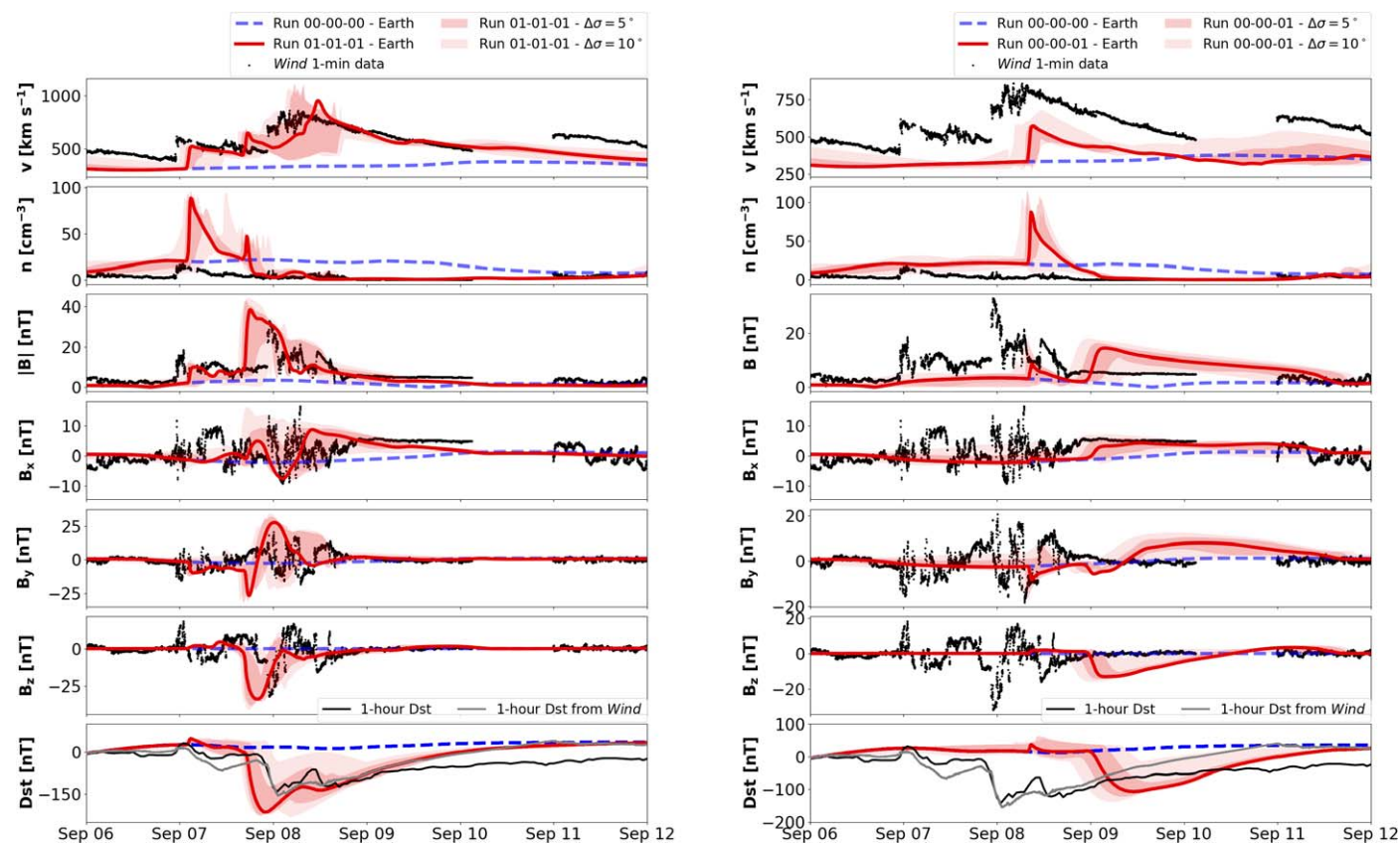


**Figure 20.** Comparison of EUHFORIA time series (red and blue) with in situ measurements from *Wind* (black) for the whole temporal computational domain (both in GSE coordinates). The bottom panel shows a comparison of the measured Dst index (black) with predictions obtained from solar wind measurements at *Wind* (gray) and from EUHFORIA time series after conversion into GSM coordinates (red and blue).

### ORCID iDs

Camilla Scolini <https://orcid.org/0000-0002-5681-0526>  
 Emmanuel Chané <https://orcid.org/0000-0001-5953-0370>  
 Manuela Temmer <https://orcid.org/0000-0003-4867-7558>  
 Emilia K. J. Kilpua <https://orcid.org/0000-0002-4489-8073>  
 Karin Dissauer <https://orcid.org/0000-0001-5661-9759>  
 Astrid M. Veronig <https://orcid.org/0000-0003-2073-002X>  
 Erika Palmerio <https://orcid.org/0000-0001-6590-3479>  
 Jens Pomoell <https://orcid.org/0000-0003-1175-7124>  
 Mateja Dumbović <https://orcid.org/0000-0002-8680-8267>  
 Jingnan Guo <https://orcid.org/0000-0002-8707-076X>  
 Luciano Rodriguez <https://orcid.org/0000-0002-6097-374X>  
 Stefaan Poedts <https://orcid.org/0000-0002-1743-0651>

### References

Altschuler, M. D., & Newkirk, G. 1969, *SoPh*, **9**, 131  
 Arge, C. N., Luhmann, J. G., Odstrcil, D., Schrijver, C. J., & Li, Y. 2004, *JASTP*, **66**, 1295  
 Bemporad, A., Zuccarello, F. P., Jacobs, C., Mierla, M., & Poedts, S. 2012, *SoPh*, **281**, 223  
 Bothmer, V., & Schwenn, R. 1998, *AnGeo*, **16**, 1  
 Brueckner, G. E., Howard, R. A., Koomen, M. J., et al. 1995, *SoPh*, **162**, 357  
 Bruno, A., Christian, E. R., de Nolfo, G. A., Richardson, I. G., & Ryan, J. M. 2019, *SpWea*, **17**, 419  
 Burt, J., & Smith, B. 2012, in Proc. IEEE Aerospace Conf., ed. D. Woerner et al. (Piscataway, NJ: IEEE), doi:10.1109/AERO.2012.6187025  
 Cane, H. V., & Richardson, I. G. 2003, *JGRA*, **108**, 1156  
 Cargill, P. J. 2004, *SoPh*, **221**, 135  
 Chandra, R., Parlat, E., Schmieder, B., Mandrini, C. H., & Uddin, W. 2010, *SoPh*, **261**, 127  
 Chatterjee, P., & Fan, Y. 2013, *ApJL*, **778**, L8

Cheng, J. X., Fang, C., & Chen, P. F. 2006, *AdSpR*, **38**, 470  
 Chertok, I. M., Belov, A. V., & Abunin, A. A. 2018, *SpWea*, **16**, 1549  
 Crooker, N. U., Gosling, J. T., & Kahler, S. W. 1998, *JGRA*, **103**, 301  
 Dasso, S., Nakwacki, M. S., Démoulin, P., & Mandrini, C. H. 2007, *SoPh*, **244**, 115  
 Démoulin, P., & Parlat, E. 2009, *AdSpR*, **43**, 1013  
 Dissauer, K., Veronig, A. M., Temmer, M., Podladchikova, T., & Vanninathan, K. 2018a, *ApJ*, **863**, 169  
 Dissauer, K., Veronig, A. M., Temmer, M., Podladchikova, T., & Vanninathan, K. 2018b, *ApJ*, **855**, 137  
 Domingo, V., Fleck, B., & Poland, A. I. 1995, *SoPh*, **162**, 1  
 Farrugia, C. J., Freeman, M. P., Burlaga, L. F., Lepping, R. P., & Takahashi, K. 1993, *JGRA*, **98**, 7657  
 Farrugia, C. J., Jordanova, V. K., Thomsen, M. F., et al. 2006, *JGRA*, **111**, A11104  
 Feng, X. 2020, *Magnetohydrodynamic Modeling of the Solar Corona and Heliosphere* (Singapore: Springer)  
 Freeland, S. L., & Handy, B. N. 1998, *SoPh*, **182**, 497  
 Gopalswamy, N., Yashiro, S., Akiyama, S., & Xie, H. 2017, *SoPh*, **292**, 65  
 Gosling, J. T. 1993, *JGRA*, **98**, 18937  
 Gosling, J. T., McComas, D. J., Phillips, J. L., & Bame, S. J. 1991, *JGRA*, **96**, 7831  
 Green, L. M., Török, T., Vršnak, B., Manchester, W., & Veronig, A. 2018, *SSRv*, **214**, 46  
 Gulisano, A. M., Démoulin, P., Dasso, S., Ruiz, M. E., & Marsch, E. 2010, *A&A*, **509**, A39  
 Hale, G. E., Ellerman, F., Nicholson, S. B., & Joy, A. H. 1919, *ApJ*, **49**, 153  
 Howard, R. A., Moses, J. D., Vourlidas, A., et al. 2008, *SSRv*, **136**, 67  
 Huttunen, K. E. J., Schwenn, R., Bothmer, V., & Koskinen, H. E. J. 2005, *AnGeo*, **23**, 625  
 Isavnin, A., Vourlidas, A., & Kilpua, E. K. J. 2014, *SoPh*, **289**, 2141  
 Kaiser, M. L., Kucera, T. A., Davila, J. M., et al. 2008, *SSRv*, **136**, 5  
 Kamide, Y., Yokoyama, N., Gonzalez, W., et al. 1998, *JGRA*, **103**, 6917  
 Kay, C., Opher, M., & Evans, R. M. 2015, *ApJ*, **805**, 168  
 Kazachenko, M. D., Lynch, B. J., Welsch, B. T., & Sun, X. 2017, *ApJ*, **845**, 49  
 Kilpua, E., Koskinen, H. E. J., & Pulkkinen, T. I. 2017a, *LRS*, **14**, 5

- Kilpua, E. K. J., Balogh, A., von Steiger, R., & Liu, Y. D. 2017b, *SSRv*, **212**, 1271
- Kilpua, E. K. J., Isavnin, A., Vourlidas, A., Koskinen, H. E. J., & Rodriguez, L. 2013, *AnGeo*, **31**, 1251
- Kilpua, E. K. J., Jian, L. K., Li, Y., Luhmann, J. G., & Russell, C. T. 2011, *JASTP*, **73**, 1228
- Koskinen, H. E. J., & Huttunen, K. E. J. 2006, *SSRv*, **124**, 169
- Künzel, H. 1965, *AN*, **288**, 177
- Lemen, J. R., Tittle, A. M., Akin, D. J., et al. 2012, *SoPh*, **275**, 17
- Lepping, R. P., Acuña, M. H., Burlaga, L. F., et al. 1995, *SSRv*, **71**, 207
- Liu, L., Wang, Y., Liu, R., et al. 2017, *ApJ*, **844**, 141
- Liu, Y., Richardson, J. D., & Belcher, J. W. 2005, *P&SS*, **53**, 3
- Liu, Y. D., Luhmann, J. G., Kajdič, P., et al. 2014a, *NatCo*, **5**, 3481
- Liu, Y. D., Yang, Z., Wang, R., et al. 2014b, *ApJL*, **793**, L41
- Lugaz, N., Farrugia, C. J., Manchester, W. B. I., & Schwadron, N. 2013, *ApJ*, **778**, 20
- Lugaz, N., Farrugia, C. J., Smith, C. W., & Paulson, K. 2015, *JGRA*, **120**, 2409
- Lugaz, N., Kintner, P., Möstl, C., et al. 2012, *SoPh*, **279**, 497
- Lugaz, N., Manchester, W. B. I., & Gombosi, T. I. 2005, *ApJ*, **634**, 651
- Lugaz, N., Manchester, W. B. I., Roussev, I. I., Tóth, G., & Gombosi, T. I. 2007, *ApJ*, **659**, 788
- Lugaz, N., Temmer, M., Wang, Y., & Farrugia, C. J. 2017, *SoPh*, **292**, 64
- Lynch, B. J., Antiochos, S. K., Li, Y., Luhmann, J. G., & DeVore, C. R. 2009, *ApJ*, **697**, 1918
- Maričić, D., Vršnak, B., Dumbović, M., et al. 2014, *SoPh*, **289**, 351
- Marubashi, K., & Lepping, R. P. 2007, *AnGeo*, **25**, 2453
- Mitra, P. K., Joshi, B., Prasad, A., Veronig, A. M., & Bhattacharyya, R. 2018, *ApJ*, **869**, 69
- Möstl, C., Amla, K., Hall, J. R., et al. 2014, *ApJ*, **787**, 119
- Möstl, C., Miklenic, C., Farrugia, C. J., et al. 2008, *AnGeo*, **26**, 3139
- Möstl, C., Temmer, M., Rollett, T., et al. 2010, *GeoRL*, **37**, L24103
- Müller, D., Nicula, B., Felix, S., et al. 2017, *A&A*, **606**, A10
- Mulligan, T., Russell, C. T., Anderson, B. J., et al. 1999, *JGRA*, **104**, 28217
- Mulligan, T., Russell, C. T., & Luhmann, J. G. 1998, *GeoRL*, **25**, 2959
- O'Brien, T. P., & McPherron, R. L. 2000a, *JGRA*, **105**, 7707
- O'Brien, T. P., & McPherron, R. L. 2000b, *JASTP*, **62**, 1295
- Odstrcil, D., Vandas, M., Pizzo, V. J., & MacNeice, P. 2003, in *AIP Conf. Ser.* **679**, Solar Wind Ten, ed. M. Velli (Melville, NY: AIP), 699
- Ogilvie, K. W., Chornay, D. J., Fritzenreiter, R. J., et al. 1995, *SSRv*, **71**, 55
- Ogilvie, K. W., & Desch, M. D. 1997, *AdSpR*, **20**, 559
- Owens, M. J. 2016, *ApJ*, **818**, 197
- Pal, S., Gopalswamy, N., Nandy, D., et al. 2017, *ApJ*, **851**, 123
- Pal, S., Nandy, D., Srivastava, N., Gopalswamy, N., & Panda, S. 2018, *ApJ*, **865**, 4
- Palmerio, E., Kilpua, E. K. J., James, A. W., et al. 2017, *SoPh*, **292**, 39
- Palmerio, E., Kilpua, E. K. J., Möstl, C., et al. 2018, *SpWea*, **16**, 442
- Pesnell, W. D., Thompson, B. J., & Chamberlin, P. C. 2012, *SoPh*, **275**, 3
- Pomoell, J., & Poedts, S. 2018, *JSWSC*, **8**, A35
- Price, D. J., Pomoell, J., Lumme, E., & Kilpua, E. K. J. 2019, *A&A*, **628**, A114
- Qiu, J., Hu, Q., Howard, T. A., & Yurchyshyn, V. B. 2007, *ApJ*, **659**, 758
- Redmon, R. J., Seaton, D. B., Steenburgh, R., He, J., & Rodriguez, J. V. 2018, *SpWea*, **16**, 1190
- Richardson, I. G., & Cane, H. V. 2010, *SoPh*, **264**, 189
- Richardson, I. G., & Cane, H. V. 2012, *JSWSC*, **2**, A02
- Riley, P., Mays, M. L., Andries, J., et al. 2018, *SpWea*, **16**, 1245
- Robbrecht, E., Berghmans, D., & Van der Linden, R. A. M. 2009, *ApJ*, **691**, 1222
- Savani, N. P., Vourlidas, A., Richardson, I. G., et al. 2017, *SpWea*, **15**, 441
- Savani, N. P., Vourlidas, A., Szabo, A., et al. 2015, *SpWea*, **13**, 374
- Scherer, P. H., Schou, J., Bush, R. I., et al. 2012, *SoPh*, **275**, 207
- Schmidt, J., & Cargill, P. 2004, *AnGeo*, **22**, 2245
- Scolini, C., Rodriguez, L., Mierla, M., Pomoell, J., & Poedts, S. 2019, *A&A*, **626**, A122
- Shen, C., Xu, M., Wang, Y., Chi, Y., & Luo, B. 2018, *ApJ*, **861**, 28
- Shen, F., Wang, Y., Shen, C., & Feng, X. 2017, *SoPh*, **292**, 104
- SunPy Community, Mumford, S. J., Christe, S., et al. 2015, *CS&D*, **8**, 014009
- Temmer, M., & Nitta, N. V. 2015, *SoPh*, **290**, 919
- Temmer, M., Reiss, M. A., Nikolic, L., Hofmeister, S. J., & Veronig, A. M. 2017, *ApJ*, **835**, 141
- Thernisien, A. 2011, *ApJS*, **194**, 33
- Thernisien, A., Howard, R. A., & Vourlidas, A. 2006, *ApJ*, **652**, 763
- Thernisien, A., Vourlidas, A., & Howard, R. A. 2009, *SoPh*, **256**, 111
- Thompson, W. T. 2006, *A&A*, **449**, 791
- Török, T., Panasenco, O., Titov, V. S., et al. 2011, *ApJL*, **739**, L63
- Tschernitz, J., Veronig, A. M., Thalmann, J. K., Hinterreiter, J., & Pötzi, W. 2018, *ApJ*, **853**, 41
- Tsurutani, B. T., Gonzalez, W. D., Tang, F., Akasofu, S. I., & Smith, E. J. 1988, *JGRA*, **93**, 8519
- Vandas, M., Fischer, S., Dryer, M., et al. 1997, *JGRA*, **102**, 22295
- Vennerstrom, S., Lefevre, L., Dumbović, M., et al. 2016, *SoPh*, **291**, 1447
- Verbeke, C., Mays, M. L., Temmer, M., et al. 2019a, *SpWea*, **17**, 6
- Verbeke, C., Pomoell, J., & Poedts, S. 2019b, *A&A*, **627**, A111
- Vourlidas, A., Colaninno, R., Nieves-Chinchilla, T., & Stenborg, G. 2011, *ApJL*, **733**, L23
- Vršnak, B., Žic, T., Vrbanec, D., et al. 2013, *SoPh*, **285**, 295
- Wang, Y., Liu, L., Shen, C., et al. 2013, *ApJL*, **763**, L43
- Werner, A. L. E., Yordanova, E., Dimmock, A. P., & Temmer, M. 2019, *SpWea*, **17**, 357
- Wold, A. M., Mays, M. L., Taktakishvili, A., et al. 2018, *JSWSC*, **8**, A17
- Xiong, M., Zheng, H., & Wang, S. 2009, *JGRA*, **114**, A11101
- Xiong, M., Zheng, H., Wang, Y., & Wang, S. 2006, *JGRA*, **111**, A08105
- Xiong, M., Zheng, H., Wu, S. T., Wang, Y., & Wang, S. 2007, *JGRA*, **112**, A11103
- Yan, X. L., Wang, J. C., Pan, G. M., et al. 2018, *ApJ*, **856**, 79
- Yashiro, S., Gopalswamy, N., Michalek, G., et al. 2004, *JGRA*, **109**, A07105
- Yurchyshyn, V. 2008, *ApJL*, **675**, L49
- Zhang, J., Richardson, I. G., Webb, D. F., et al. 2007, *JGRA*, **112**, A10102
- Zhang, J., & Wang, J. 2002, *ApJL*, **566**, L117